

A high order discontinuous Galerkin method for the symmetric form of the anisotropic viscoelastic wave equation

Khemraj Shukla*, Jesse Chan, Maarten V. de Hoop

Department of Computational and Applied Mathematics, Rice University, 6100 Main St, Houston, TX, 77005

Abstract

Wave propagation in real media is affected by various non-trivial physical phenomena, e.g., anisotropy, an-elasticity and dissipation. Assumptions on the stress-strain relationship are an integral part of seismic modeling and determine the deformation and relaxation of the medium. Stress-strain relationships based on simplified rheologies will incorrectly predict seismic amplitudes, which are used for quantitative reservoir characterization. Constitutive equations for the rheological model include the generalized Hooke's law and Boltzmann's superposition principal with dissipation models based on standard linear solids or a Zener approximation.

In this work, we introduce a high-order discontinuous Galerkin finite element method for wave equation in inhomogeneous and anisotropic dissipative medium. This method is based on a new symmetric treatment of the anisotropic viscoelastic terms, as well as an appropriate memory variable treatment of the stress-strain convolution terms. Together, these result in a symmetric system of first order linear hyperbolic partial differential equations. The accuracy of the proposed numerical scheme is proven and verified using convergence studies against analytical plane wave solutions and analytical solutions of viscoelastic wave equation. Computational experiments are shown for various combinations of homogeneous and heterogeneous viscoelastic media in two and three dimensions.

1. Introduction

Numerical simulations of seismic wave propagation are essential for various imaging problems arising at different scales. At a global scale, seismic waves, traveling thorough the entire Earth allow geophysicists to infer properties of the Earth interior. At a macro-scale, seismic wave propagation can be used to image and characterize oil and gas reservoirs. On a micro or laboratory scale, seismic waves play a major role in studying the micro-structure of materials. To simulate wave propagation accurately, the input model should be able to accommodate arbitrary variations of petrophysical and lithological properties, as they play an important role, particularly in the targets of exploration geophysics, i.e., reservoir rocks. To study reservoir monitoring and evaluation of rock properties in a laboratory setting, lithological and reservoir properties become more important. Reservoir rocks such as cracked limestones can show effective anisotropy in the seismic band. Furthermore, fluid-filled cracked rocks and porous sandstones show considerable attenuation properties. Experimental work also shows that anisotropy effects of attenuation are more pronounced than anisotropic elastic effects [1, 2]. Thus, a realistic rheology should be able to model anisotropic attenuation characteristics.

Various dissipation mechanisms (e.g. Kelvin-Voigt, Maxwell, Zener [3]) can be modeled by a viscoelastic constitutive relation. Attenuation of energy is caused by a large variety of dissipation mechanisms. it is difficult, if not impossible, to build a general microstructure theory incorporating all these mechanisms.

*corresponding author

Email addresses: rajexplo@gmail.com (Khemraj Shukla), jesse.chan@rice.edu (Jesse Chan), mdehoop@rice.edu (Maarten V. de Hoop)

Modeling of dissipation in isotropic media requires two relaxation functions. These two relaxation functions are enough to describe anelastic characteristics of body waves because these modes decouple in a homogeneous medium with isotropic attenuation [4]. In contrast, in anisotropic media, one has to decide the time (or frequency) dependence of 21 stiffness parameters. However, Mehrabadi and Cowin [5] and Helbig [6] show that only six of the 21 stiffness parameters have an intrinsic physical meaning.

Motivated by the works of Mehrabadi and Cowin [5] and Helbig [6], Carcione formulated a constitutive model and wave equations for linear viscoelastic anisotropic media [7]. In three-dimensional anisotropic media, careful attention is required for modeling properties of the shear modes, since the relaxation of a medium can be different for slow and fast waves. Carcione used a relaxation function to model the anelastic properties of the quasi-dilatational mode, whereas three relaxation functions are used to control the relaxation of the medium due to the shear waves along preferred directions. In this study, we use the constitutive model proposed by Carcione [4] and pair it with equations of motion described by Newton’s second law of motion. This results in a system of first order hyperbolic PDEs with stress-velocity field variables.

Numerical simulations of seismic wave propagation solve the system of hyperbolic partial differential equations using various numerical methods such as finite-differences, finite volumes and finite element methods. An overview of these methods is given by [8, 9]. The most popular and simple method is the finite-difference (FD) method, and its application to the elastic wave equation has been studied by many researchers [10, 11, 12, 13, 14]. A detailed analysis of finite-difference methods is given in [15]. Although the numerical representation of FD method is very simple, it often comes with significant numerical dispersion, especially in the modeling of surface waves [11]. Additionally, the implementation of boundary conditions can require special treatment [16]. FD methods are also difficult to apply to irregular geometries without experiencing “staircase effects” [16]. To circumvent the effect of numerical dispersion and achieve high order accuracy, pseudo-spectral methods were first used by Tessmer and Kosloff [17]. The pseudo-spectral method uses global basis function for approximation of the solutions (e.g., Fourier or Chebyshev). The pseudo-spectral method requires few grid points per wavelength and produces a high order solution with less numerical dispersion. However, the choice of the global basis functions restricts the pseudo-spectral methods to smooth models, as it is difficult to represent materials with the discontinuities or sharp contrast. This can be addressed somewhat using domain decomposition, where different meshes are used to represent the different domains. For example, Carcione [18] used Fourier basis functions along directions with smoothly varying materials properties and Chebyshev basis functions in directions with sharply varying medium properties.

The finite element method (FEM) method discretizes the domain using elements (e.g., triangles and quadrilaterals in 2D and tetrahedra and hexahedra in 3D). Since time-domain wave propagation is described by a hyperbolic system of partial differential equations, an explicit time integration can efficiently be applied. However, finite-element methods, when coupled with an explicit time integrator, require the inversion of a global mass matrix unless special techniques (such as diagonal mass lumping) are applied. Finite elements for elastic wave propagation were studied by Marfurt [11] and Bao *et al.* [19]. In these works, FEM was shown to accurately represent sharp material properties and irregular geometries. However, the solution on each element is approximated using a low order polynomial, which results in significant numerical dispersion. In order to recover a more accurate solution, high order elements are required which results into large matrices to be inverted at each time step. To exploit the spectral properties in the finite element method Patera [20] proposed the spectral element method (SEM) to solve fluid flow problems. Subsequently, the SEM was successfully implemented by Seriani *et al.* [21] to solve the acoustic wave equation in a heterogeneous medium. Komatitsch and Vilotte [22] used SEM to solve the elastic wave equation in a heterogeneous medium, described by a system of the second order PDEs. A detailed review of seismic modeling is presented Carcione *et al.* [23].

In the present study, we introduce a high-order numerical scheme based on the discontinuous Galerkin method to solve the 3D viscoelastic wave equation on unstructured tetrahedral meshes. High order methods provide one avenue towards improving fidelity in numerical simulations while maintaining reasonable computational costs, and methods which can accommodate unstructured meshes are desirable for problems with complex geometries. Among such methods, high order discontinuous Galerkin (DG) methods are particularly well-suited to the solution of time-dependent hyperbolic problems on modern computing architectures

[24, 25]. The accuracy of high order methods can be attributed in part to their low numerical dissipation and dispersion compared to low order schemes [26]. This accuracy has made them advantageous for the simulation of electro-magnetic and elastic wave propagation [24, 27]. Spectral element methods avoid the inversion of the global mass matrix for quadrilateral and hexahedral elements by choosing nodal basis functions, which are discretely orthogonal with respect to an under-integrated L^2 inner product and result in a diagonal mass matrix [22]. In contrast, high order DG methods produce block diagonal mass matrices, which are locally invertible. High order DG methods are often used for seismic simulation (elastic approximation) in combination with simplicial meshes [28, 29, 30].

DG methods impose inter-element continuity of approximate solutions between elements weakly through a numerical flux, of which the upwind flux (solution of a Riemann problem) is more common. Käser *et al.* [28] solved the 3D isotropic viscoelastic wave equation in a strain-velocity formulation using a local space-time DG method with an upwind flux by solving the exact Riemann problem on inter-element boundaries. In another study, Lambrecht *et al.* [31] used a nodal DG method to solve the isotropic viscoelastic wave equation using the same formulation proposed by Käser *et al.* [28]. The solution of the Riemann problem requires diagonalization of Jacobian matrices into polarized waves constituents, which is a computationally intensive process for the viscoelastic system and does not extend naturally to anisotropic materials. Ye *et al.* [30] completely avoids the process of diagonalization for the coupled acoustic-elastic wave equation by using a penalty flux based on natural boundary conditions. In this study, we use a similar energy-stable penalty flux for the anisotropic viscoelastic wave equations.

The main new contributions of this paper are a new symmetric form of the anisotropic viscoelastic wave equation and its discretization using a high order DG method using penalty fluxes. The outline of the paper is as follows: Section 2 will discuss the system of equations describing the viscoelastic wave equation. Section 3 presents an energy stable formulation for the symmetric hyperbolic form of the viscoelastic wave equations. Finally, numerical results in Section 4 demonstrate the accuracy of this method for several problems in linear anisotropic viscoelasticity.

2. Constitutive Relations

2.1. Notation and convention

Let f and g be scalar and time-dependent functions. The Riemann convolution of f with g is defined as

$$f * g = \begin{cases} \int_0^t f(\tau)g(t-\tau) d\tau : & t \geq 0 \\ 0 : & t < 0, \end{cases} \quad (1)$$

where t is the time variable. Hooke's law is expressed in 3-D or 6-D space depending on whether stress or strain are considered as tensors or vectors, and the convolution shown by (1) is easily extended to include vectors and tensors as follows

$$\mathbf{\Psi} * \mathbf{A} = \int_0^t \mathbf{\Psi}(\tau) \cdot \mathbf{A}(t-\tau) d\tau \quad (2)$$

where \mathbf{A} and $\mathbf{\Psi}$ are 6×6 stress (strain) tensor and $\mathbf{\Psi}$ are relaxation matrices.

If f and g are of Heaviside type, the Boltzman operation [32] defines the time derivative of the convolution between f and g as

$$f * \partial_t g = f \odot g = \mathring{f}g + (\mathring{f}H) * g, \quad (3)$$

where $\mathring{f} = f(t=0) = f(t=0^+)$ and $H(t)$ is the step function. Sub-indices i, j, k , and m take values from 1 to 3 and correspond to the three Cartesian coordinates x, y and z .

2.2. Boltzmann law

The general constitutive relation for an anisotropic and linear viscoelastic medium can be expressed as [4]

$$\boldsymbol{\sigma} = \dot{\boldsymbol{\Psi}} * \boldsymbol{\epsilon} \quad (4)$$

where $\boldsymbol{\sigma} = [\sigma_{11}, \sigma_{22}, \sigma_{22}, \sigma_{23}, \sigma_{13}, \sigma_{12}]^T$, $\boldsymbol{\epsilon} = [\epsilon_{11}, \epsilon_{22}, \epsilon_{33}, \epsilon_{23}, \epsilon_{13}, \epsilon_{12}]^T$ are stress and strain vectors with $\gamma_{ij} = 2\epsilon_{ij}$, and $\boldsymbol{\Psi}$ is the symmetric relaxation matrix.

The stress-strain relation in (4) is called the Boltzmann law and can be expressed as more explicitly by using the Einstein notation of summation over repeated indices

$$\sigma_I = \psi_{IJ} * \dot{\epsilon}_J, \quad I, J = 1, \dots, 6 \quad (5)$$

To model the anelastic properties of shear waves, Carcione [7] used one relaxation function for quasi dilatational mode and three relaxation functions for shear modes and expressed relaxation matrix $\boldsymbol{\Psi}$ as

$$\boldsymbol{\Psi} = \begin{bmatrix} \psi_{11} & \psi_{12} & \psi_{13} & c_{14} & c_{15} & c_{16} \\ & \psi_{22} & \psi_{23} & c_{24} & c_{25} & c_{26} \\ & & \psi_{33} & c_{34} & c_{35} & c_{36} \\ & & & c_{44}\chi_2 & c_{45} & c_{46} \\ & & & & c_{55}\chi_3 & c_{56} \\ & & & & & c_{66}\chi_4 \end{bmatrix} H(t), \quad (6)$$

where

$$\psi_{i(I)} = c_{I(I)} - D + K\chi_1 + \frac{4}{3}G\chi_\delta \quad \text{for } I = 1, 2, 3, \quad (7)$$

$$\psi_{IJ} = c_{IJ} - D + 2G + K\chi_1 - \frac{2}{3}G\chi_\delta \quad \text{for } I, J = 1, 2, 3; I \neq J. \quad (8)$$

The C_{IJ} for $I, J = 1, \dots, 6$ are the high-frequency limit (relaxed) elasticities i.e. $t \rightarrow 0; \omega \rightarrow \infty$, and

$$K = D - \frac{4}{3}G, \quad (9)$$

where

$$D = \frac{1}{3}(c_{11} + c_{22} + c_{33}), \quad G = \frac{1}{3}(c_{44} + c_{55} + c_{66}).$$

The χ_ν are dimensionless relaxation function with index $\nu = 1$ representing the quasi-dilatational mode and indices $\nu = 2, 3, 4$ corresponds to shear waves. In (7), (8) and (9), χ_δ is a shear relaxation function for $\delta = 2, 3$, or 4. $H(t)$ is the Heaviside function.

The relaxation matrix shown in (6) generalizes the anisotropic relaxation model (4) as three relaxation functions are used to describe anelastic properties of shear modes. This also allows for the control of the dissipation of energy along three preferred directions e.g. the principal axes of the anisotropic medium.

The choice of the relaxation functions depends on the symmetry system of the material, since attenuation symmetries follow the symmetry of the crystallographic form of material [4]. In this study, the following relaxation functions are used [3]

$$\chi_\nu(t) = L_\nu \left(\sum_{l=1}^{L_\nu} \frac{\tau_{el}^{(\nu)}}{\tau_{\sigma l}^{(\nu)}} \right) \left[1 - \frac{1}{L_\nu} \sum_{l=1}^{L_\nu} \left(1 - \frac{\tau_{el}^{(\nu)}}{\tau_{\sigma l}^{(\nu)}} \right) \exp \left(-t/\tau_{\sigma l}^{(\nu)} \right) \right], \quad \nu = 1, \dots, 4, \quad (10)$$

where $\tau_{el}^{(\nu)}$ and $\tau_{\sigma l}^{(\nu)}$ are material relaxation times such that $\tau_{el}^{(\nu)} \geq \tau_{\sigma l}^{(\nu)}$. The pair $\tau_{el}^{(\nu)}$ and $\tau_{\sigma l}^{(\nu)}$ define a dissipation mechanism.

Equation (10) describes the relaxation function of generalized standard linear solid (also known as Zener model) consisting of L_ν elements ¹ connected in parallel. The complex modulus of the system is [3]

$$M_\nu(\omega) = \mathcal{F} \left(\frac{d[\chi_\nu(t)H(t)]}{dt} \right), \quad (11)$$

where ω is the angular frequency and $\mathcal{F}(\cdot)$ represents the time Fourier transform of the variable.

$M_\nu(\omega)$ is expressed as

$$M_\nu(\omega) = \left(\sum_{l=1}^{L_\nu} \frac{\tau_{\epsilon l}^{(\nu)}}{\tau_{\sigma l}^{(\nu)}} \right) \sum_{l=1}^{L_\nu} \frac{1 + i\omega\tau_{\epsilon l}^{(\nu)}}{1 + i\omega\tau_{\sigma l}^{(\nu)}}. \quad (12)$$

From (12) it can be easily seen that $M_\nu(\omega) = 1$ as $\frac{\tau_{\epsilon l}^{(\nu)}}{\tau_{\sigma l}^{(\nu)}} \rightarrow 1$, which gives the low frequency limit. Thus, (12) is a general relaxation function which can recover all possible type of frequency behavior of attenuation and velocity dispersion observed in subsurface materials.

2.3. Strain memory variables

The time-domain stress-strain relation can be expressed as

$$\sigma_I = \psi_{IJ} * \partial_t e_J \quad (13)$$

Applying the Boltzmann operation (3) to (13), we obtain

$$\sigma_I = \dot{\psi}_{IJ} e_J + \left(\dot{\psi}_{IJ} H \right) * e_J \quad (14)$$

Now we use

$$\check{\phi}_{\nu l}(t) = \dot{\chi}_\nu(t) = \frac{1}{\tau_{\sigma l}^{(\nu)}} \left(\sum_{l=1}^{L_\nu} \frac{\tau_{\epsilon l}^{(\nu)}}{\tau_{\sigma l}^{(\nu)}} \right) \left(1 - \frac{\tau_{\epsilon l}^{(\nu)}}{\tau_{\sigma l}^{(\nu)}} \right) \exp \left(-t/\tau_{\sigma l}^{(\nu)} \right)$$

and write (14) in matrix form, which is expressed as

$$\sigma_I = A_{IJ}^{(\nu)} e_J + B_{IJ}^{(\nu)} \sum_{l=1}^{L_\nu} e_{Jl}^{(\nu)}, \quad (15)$$

where A 's and B 's are the matrices formed by the combination of elastic constants c_{IJ} and

$$e_{Jl}^{(\nu)} = \phi_{\nu l}(t) * e_J, \quad J = 1, \dots, 6, \quad l = 1, \dots, L_\nu, \quad \nu = 1, \dots, 4,$$

where $\phi_{\nu l} = \check{\phi}_{\nu l}(t)H(t)$ are the components of 6×1 strain memory array $\mathbf{e}_l^{(\nu)}$.

In 3D, the symmetric strain memory tensor corresponding to the l^{th} dissipation mechanism of the relaxation function χ_ν is expressed as [7]

$$\mathbf{e}_l^{(\nu)} = \begin{bmatrix} e_{11l}^{(\nu)} & e_{12l}^{(\nu)} & e_{13l}^{(\nu)} \\ & e_{22l}^{(\nu)} & e_{23l}^{(\nu)} \\ & & e_{33l}^{(\nu)} \end{bmatrix} = \phi_{\nu l} * \begin{bmatrix} \epsilon_{11} & \gamma_{12} & \gamma_{13} \\ & \epsilon_{22} & \gamma_{23} \\ & & \epsilon_{33} \end{bmatrix} \quad (16)$$

$$= \phi_{\nu l}(t) * e_J. \quad (17)$$

¹A mechanical system in which a spring and a parallel combination of a dashpot and a spring are connected in series.

The tensor $\mathbf{e}_l^{(\nu)}$ contains the past history of material due the dissipation mechanism defined in (10). In the pure elastic case $\tau_{el}^{(\nu)} \rightarrow \tau_{\sigma l}^{(\nu)}$, $\phi_{\nu l} \rightarrow 0$ and $\mathbf{e}_l^{(\nu)}$ vanishes.

Similar to the strain tensor, the memory strain variable can be decomposed as

$$\mathbf{e}_l^{(\nu)} = \mathbf{d}_l^{(\nu)} + \left(\frac{1}{3} \text{tr}(\mathbf{e}_l^{(\nu)}) \right) \mathbf{I}, \quad \text{tr}(\mathbf{d}_l^{(\nu)}) = 0, \quad (18)$$

where $\mathbf{d}_l^{(\nu)}$ is the deviatoric strain memory tensor which is traceless and \mathbf{I} is 3×3 identity matrix. Thus, the dilatation and shear memory variables are defined as

$$e_{1l} = \text{tr}(\mathbf{e}_l^{(1)}), \quad \text{and} \quad e_{ijl} = (\mathbf{d}_l^{(\nu)})_{ij}, \quad (19)$$

where $\nu = \delta$ for $i = j$, $\nu = 2$ for $ij = 23$, $\nu = 3$ for $ij = 13$ and $\nu = 4$ for $ij = 12$.

The stress-strain relations in terms of strain components and memory variables with one dissipation mechanism for each mode are [7]

$$\sigma_{11} = c_{11}\epsilon_{11} + c_{12}\epsilon_{22} + c_{13}\epsilon_{33} + c_{14}\gamma_{23} + c_{15}\gamma_{13} + c_{16}\gamma_{12} + Ke_{11} + 2Ge_{111}^{(\delta)} \quad (20a)$$

$$\sigma_{22} = c_{12}\epsilon_{11} + c_{22}\epsilon_{22} + c_{23}\epsilon_{33} + c_{24}\gamma_{23} + c_{25}\gamma_{13} + c_{26}\gamma_{12} + Ke_{11} + 2Ge_{221}^{(\delta)} \quad (20b)$$

$$\sigma_{33} = c_{13}\epsilon_{11} + c_{23}\epsilon_{22} + c_{33}\epsilon_{33} + c_{34}\gamma_{23} + c_{35}\gamma_{13} + c_{36}\gamma_{12} + Ke_{11} - 2G(e_{111}^{(\delta)} + e_{221}^{(\delta)}) \quad (20c)$$

$$\sigma_{23} = c_{14}\epsilon_{11} + c_{24}\epsilon_{22} + c_{34}\epsilon_{33} + c_{44}\gamma_{23} + c_{44}e_{231}^{(2)} + c_{45}\gamma_{13} + c_{46}\gamma_{12} \quad (20d)$$

$$\sigma_{13} = c_{15}\epsilon_{11} + c_{25}\epsilon_{22} + c_{35}\epsilon_{33} + c_{45}\gamma_{23} + c_{55}\gamma_{23} + c_{55}e_{131}^{(3)} + c_{56}\gamma_{12} \quad (20e)$$

$$\sigma_{12} = c_{16}\epsilon_{11} + c_{26}\epsilon_{22} + c_{36}\epsilon_{33} + c_{46}\gamma_{23} + c_{56}\gamma_{13} + c_{66}\gamma_{13} + c_{66}e_{121}^{(4)} \quad (20f)$$

$$(20g)$$

where $c_{IJ} = \psi_{IJ}(t = 0^+)$ are unrelaxed elasticity constant at $\omega \rightarrow \infty$.

2.4. Memory variable equation

Applying the Boltzman equation to the deviatoric part of (17) yields

$$\partial_t \mathbf{d}_l^{(\nu)} = \phi_{\nu l}(0) \mathbf{d} + (\partial_t \check{\phi}_{\nu l} H) * \mathbf{d}. \quad (21)$$

Here, \mathbf{d} denotes the deviatoric strain tensor with elements

$$\mathbf{d} = \boldsymbol{\epsilon} - \frac{1}{3} \mathcal{V} \mathbf{I}, \quad (22)$$

where the strain tensor $\boldsymbol{\epsilon}$ and \mathcal{V} are

$$\boldsymbol{\epsilon} = \begin{bmatrix} \epsilon_{11} & \epsilon_{12} & \epsilon_{13} \\ \epsilon_{12} & \epsilon_{22} & \epsilon_{23} \\ \epsilon_{13} & \epsilon_{23} & \epsilon_{33} \end{bmatrix}, \quad \mathcal{V} = \epsilon_{11} + \epsilon_{22} + \epsilon_{33}.$$

Using $\partial_t \check{\phi}_{\nu l} = -\frac{\check{\phi}_{\nu l}}{\tau_{\sigma l}^{(\nu)}}$ and substituting it in (21), we recover

$$\partial_t \mathbf{d}_l^{(\nu)} = \phi_{\nu l}(0) \mathbf{d} - \frac{1}{\tau_{\sigma l}^{(\nu)}} \mathbf{d}_l^{(\nu)}, \quad (23)$$

where $\mathbf{d}_l^{(\nu)} = \phi_{\nu l}(t) * \mathbf{d}$, with $\nu = 2, 3$, and 4. Similarly applying the Boltzmann operation to the non-deviatoric part $\text{tr}(\mathbf{e}_l^{(1)})$, we get

$$\partial_t \text{tr}(\mathbf{e}_l^{(1)}) = \phi_{1l}(0) \text{tr}(\mathbf{e}) - \frac{1}{\tau_{\sigma l}^{(1)}} \text{tr}(\mathbf{e}_l^{(1)}) \quad (24)$$

Using (23) and (24), The equations for the memory variables are expressed as

$$\partial_t e_{111}^{(\delta)} = \phi_{\delta 1}(0)(\epsilon_{11} - \bar{\epsilon}) - \frac{e_{111}^{(\delta)}}{\tau_{\sigma}^{(\delta)}} \quad (25a)$$

$$\partial_t e_{221}^{(\delta)} = \phi_{\delta 1}(0)(\epsilon_{22} - \bar{\epsilon}) - \frac{e_{221}^{(\delta)}}{\tau_{\sigma}^{(\delta)}} \quad (25b)$$

$$\partial_t e_{231} = \phi_{21}(0)\gamma_{23} - \frac{e_{231}}{\tau_{\sigma}^{(2)}} \quad (25c)$$

$$\partial_t e_{131} = \phi_{31}(0)\gamma_{13} - \frac{e_{131}}{\tau_{\sigma}^{(3)}} \quad (25d)$$

$$\partial_t e_{121} = \phi_{41}(0)\gamma_{12} - \frac{e_{121}}{\tau_{\sigma}^{(4)}} \quad (25e)$$

$$\partial_t e_{11} = n\phi_{1l}(0)\bar{\epsilon} - e_{11}/\tau_{\sigma}^{(1)} \quad (25f)$$

where $\bar{\epsilon} = \text{tr}(\mathbf{S})/3$ and n is taken as 2 for 2D and 3 for 3D.

2.5. Equation of motion

The conservation of momentum is expressed as

$$\frac{\partial \sigma_{11}}{\partial x_1} + \frac{\partial \sigma_{12}}{\partial x_2} + \frac{\partial \sigma_{13}}{\partial x_3} = \rho \frac{\partial v_1}{\partial t} \quad (26a)$$

$$\frac{\partial \sigma_{12}}{\partial x_1} + \frac{\partial \sigma_{22}}{\partial x_2} + \frac{\partial \sigma_{23}}{\partial x_3} = \rho \frac{\partial v_2}{\partial t} \quad (26b)$$

$$\frac{\partial \sigma_{13}}{\partial x_1} + \frac{\partial \sigma_{23}}{\partial x_2} + \frac{\partial \sigma_{33}}{\partial x_3} = \rho \frac{\partial v_3}{\partial t} \quad (26c)$$

2.6. System of equations in matrix form in 3D

Let us consider the 3D-particle-velocity and stress equations for propagation in an anisotropic medium. We assign one relaxation mechanism to both dilatational anelastic deformation ($\nu = 1$) and shear anelastic deformations ($\nu = 2$). The stress-strain relation is expressed as

$$\begin{aligned} \frac{\partial \sigma_{11}}{\partial t} &= c_{11} \frac{\partial v_1}{\partial x_1} + c_{12} \frac{\partial v_2}{\partial x_2} + c_{13} \frac{\partial v_3}{\partial x_3} + K e_1 + 2G e_2, \\ \frac{\partial \sigma_{22}}{\partial t} &= c_{12} \frac{\partial v_1}{\partial x_1} + c_{11} \frac{\partial v_2}{\partial x_2} + c_{13} \frac{\partial v_3}{\partial x_3} + K e_1 + 2G e_3, \\ \frac{\partial \sigma_{33}}{\partial t} &= c_{13} \frac{\partial v_1}{\partial x_1} + c_{13} \frac{\partial v_2}{\partial x_2} + c_{33} \frac{\partial v_3}{\partial x_3} + K e_1 - 2G(e_2 + e_3) \\ \frac{\partial \sigma_{23}}{\partial t} &= c_{44} \left[\left(\frac{\partial v_2}{\partial x_3} + \frac{\partial v_3}{\partial x_2} \right) + e_4 \right], \\ \frac{\partial \sigma_{13}}{\partial t} &= c_{55} \left[\left(\frac{\partial v_1}{\partial x_3} + \frac{\partial v_3}{\partial x_1} \right) + e_5 \right], \\ \frac{\partial \sigma_{12}}{\partial t} &= c_{66} \left[\left(\frac{\partial v_1}{\partial x_2} + \frac{\partial v_2}{\partial x_1} \right) + e_6 \right]. \end{aligned} \quad (27)$$

Memory variables are expressed as

$$\begin{aligned}
\frac{\partial e_1}{\partial t} &= \frac{1}{\tau_\sigma^{(1)}} \left[\left(\frac{\tau_\sigma^{(1)}}{\tau_\epsilon^{(1)}} - 1 \right) \left(\frac{\partial v_1}{\partial x_1} + \frac{\partial v_2}{\partial x_2} + \frac{\partial v_3}{\partial x_3} \right) - e_1 \right], \\
\frac{\partial e_2}{\partial t} &= \frac{1}{3\tau_\sigma^{(2)}} \left[\left(\frac{\tau_\sigma^{(2)}}{\tau_\epsilon^{(2)}} - 1 \right) \left(2\frac{\partial v_1}{\partial x_1} - \frac{\partial v_2}{\partial x_2} - \frac{\partial v_3}{\partial x_3} \right) - 3e_2 \right], \\
\frac{\partial e_3}{\partial t} &= \frac{1}{3\tau_\sigma^{(3)}} \left[\left(\frac{\tau_\sigma^{(3)}}{\tau_\epsilon^{(3)}} - 1 \right) \left(2\frac{\partial v_2}{\partial x_2} - \frac{\partial v_1}{\partial x_1} - \frac{\partial v_3}{\partial x_3} \right) - 3e_3 \right], \\
\frac{\partial e_4}{\partial t} &= \frac{1}{\tau_\sigma^{(2)}} \left[\left(\frac{\tau_\sigma^{(2)}}{\tau_\epsilon^{(2)}} - 1 \right) \left(\frac{\partial v_2}{\partial x_3} + \frac{\partial v_3}{\partial x_2} \right) - e_4 \right], \\
\frac{\partial e_5}{\partial t} &= \frac{1}{\tau_\sigma^{(3)}} \left[\left(\frac{\tau_\sigma^{(3)}}{\tau_\epsilon^{(3)}} - 1 \right) \left(\frac{\partial v_1}{\partial x_3} + \frac{\partial v_3}{\partial x_1} \right) - e_5 \right], \\
\frac{\partial e_6}{\partial t} &= \frac{1}{\tau_\sigma^{(4)}} \left[\left(\frac{\tau_\sigma^{(4)}}{\tau_\epsilon^{(4)}} - 1 \right) \left(\frac{\partial v_1}{\partial x_2} + \frac{\partial v_2}{\partial x_1} \right) - e_6 \right].
\end{aligned} \tag{28}$$

Combining (26)-(28) in matrix form yields

$$\frac{\partial \mathbf{q}}{\partial t} + \mathbf{A}(\mathbf{x}) \frac{\partial \mathbf{q}}{\partial x_1} + \mathbf{B}(\mathbf{x}) \frac{\partial \mathbf{q}}{\partial x_2} + \mathbf{C}(\mathbf{x}) \frac{\partial \mathbf{q}}{\partial x_3} = \mathbf{D}(\mathbf{x}) \mathbf{q} + \mathbf{f}, \tag{29}$$

where

$$\mathbf{q} = [\sigma_{11}, \sigma_{22}, \sigma_{33}, \sigma_{23}, \sigma_{13}, \sigma_{12}, e_1, e_2, e_3, e_4, e_5, e_6, v_1, v_2, v_3],$$

$$\mathbf{A}(\mathbf{x}) = - \begin{bmatrix} 0 & 0 & 0 & 0 & 0 & 0 & 0 & 0 & 0 & 0 & 0 & 0 & c_{11}(\mathbf{x}) & 0 & 0 \\ 0 & 0 & 0 & 0 & 0 & 0 & 0 & 0 & 0 & 0 & 0 & 0 & c_{12}(\mathbf{x}) & 0 & 0 \\ 0 & 0 & 0 & 0 & 0 & 0 & 0 & 0 & 0 & 0 & 0 & 0 & c_{13}(\mathbf{x}) & 0 & 0 \\ 0 & 0 & 0 & 0 & 0 & 0 & 0 & 0 & 0 & 0 & 0 & 0 & 0 & 0 & 0 \\ 0 & 0 & 0 & 0 & 0 & 0 & 0 & 0 & 0 & 0 & 0 & 0 & 0 & 0 & c_{55}(\mathbf{x}) \\ 0 & 0 & 0 & 0 & 0 & 0 & 0 & 0 & 0 & 0 & 0 & 0 & 0 & c_{66}(\mathbf{x}) & 0 \\ 0 & 0 & 0 & 0 & 0 & 0 & 0 & 0 & 0 & 0 & 0 & 0 & T_1(\mathbf{x}) & 0 & 0 \\ 0 & 0 & 0 & 0 & 0 & 0 & 0 & 0 & 0 & 0 & 0 & 0 & \frac{2}{3}T_2(\mathbf{x}) & 0 & 0 \\ 0 & 0 & 0 & 0 & 0 & 0 & 0 & 0 & 0 & 0 & 0 & 0 & -\frac{1}{3}T_3(\mathbf{x}) & 0 & 0 \\ 0 & 0 & 0 & 0 & 0 & 0 & 0 & 0 & 0 & 0 & 0 & 0 & 0 & 0 & 0 \\ 0 & 0 & 0 & 0 & 0 & 0 & 0 & 0 & 0 & 0 & 0 & 0 & 0 & 0 & T_3(\mathbf{x}) \\ 0 & 0 & 0 & 0 & 0 & 0 & 0 & 0 & 0 & 0 & 0 & 0 & 0 & T_4(\mathbf{x}) & 0 \\ 1/\rho(\mathbf{x}) & 0 & 0 & 0 & 0 & 0 & 0 & 0 & 0 & 0 & 0 & 0 & 0 & 0 & 0 \\ 0 & 0 & 0 & 0 & 0 & 1/\rho(\mathbf{x}) & 0 & 0 & 0 & 0 & 0 & 0 & 0 & 0 & 0 \\ 0 & 0 & 0 & 0 & 1/\rho(\mathbf{x}) & 0 & 0 & 0 & 0 & 0 & 0 & 0 & 0 & 0 & 0 \end{bmatrix},$$

$$D(\mathbf{x}) = - \begin{bmatrix} 0 & 0 & 0 & 0 & 0 & 0 & K(\mathbf{x}) & 2G(\mathbf{x}) & 0 & 0 & 0 & 0 & 0 & 0 & 0 \\ 0 & 0 & 0 & 0 & 0 & 0 & K(\mathbf{x}) & 0 & 2G(\mathbf{x}) & 0 & 0 & 0 & 0 & 0 & 0 \\ 0 & 0 & 0 & 0 & 0 & 0 & K(\mathbf{x}) & -2G(\mathbf{x}) & -2G(\mathbf{x}) & 0 & 0 & 0 & 0 & 0 & 0 \\ 0 & 0 & 0 & 0 & 0 & 0 & 0 & 0 & 0 & c_{44}(\mathbf{x}) & 0 & 0 & 0 & 0 & 0 \\ 0 & 0 & 0 & 0 & 0 & 0 & 0 & 0 & 0 & 0 & c_{55}(\mathbf{x}) & 0 & 0 & 0 & 0 \\ 0 & 0 & 0 & 0 & 0 & 0 & 0 & 0 & 0 & 0 & 0 & c_{66}(\mathbf{x}) & 0 & 0 & 0 \\ 0 & 0 & 0 & 0 & 0 & 0 & -\frac{1}{\tau_\sigma^{(1)}(\mathbf{x})} & 0 & 0 & 0 & 0 & 0 & 0 & 0 & 0 \\ 0 & 0 & 0 & 0 & 0 & 0 & 0 & -\frac{1}{\tau_\sigma^{(2)}(\mathbf{x})} & 0 & 0 & 0 & 0 & 0 & 0 & 0 \\ 0 & 0 & 0 & 0 & 0 & 0 & 0 & 0 & -\frac{1}{\tau_\sigma^{(3)}(\mathbf{x})} & 0 & 0 & 0 & 0 & 0 & 0 \\ 0 & 0 & 0 & 0 & 0 & 0 & 0 & 0 & 0 & -\frac{1}{\tau_\sigma^{(2)}(\mathbf{x})} & 0 & 0 & 0 & 0 & 0 \\ 0 & 0 & 0 & 0 & 0 & 0 & 0 & 0 & 0 & 0 & -\frac{1}{\tau_\sigma^{(3)}(\mathbf{x})} & 0 & 0 & 0 & 0 \\ 0 & 0 & 0 & 0 & 0 & 0 & 0 & 0 & 0 & 0 & 0 & -\frac{1}{\tau_\sigma^{(4)}(\mathbf{x})} & 0 & 0 & 0 \\ 0 & 0 & 0 & 0 & 0 & 0 & 0 & 0 & 0 & 0 & 0 & 0 & 0 & 0 & 0 \\ 0 & 0 & 0 & 0 & 0 & 0 & 0 & 0 & 0 & 0 & 0 & 0 & 0 & 0 & 0 \\ 0 & 0 & 0 & 0 & 0 & 0 & 0 & 0 & 0 & 0 & 0 & 0 & 0 & 0 & 0 \end{bmatrix},$$

where $T_i = \frac{1}{\tau_\sigma^{(i)}(\mathbf{x})} \left(\frac{\tau_\sigma^{(i)}(\mathbf{x})}{\tau_\epsilon^{(i)}(\mathbf{x})} - 1 \right)$.

To prove stability of the scheme, we express (29) in a form where spatially dependent material coefficient appear on left side of (31). This will enable us to rewrite (28) without terms involving the spatial derivatives. From (27), we compute $\frac{\partial v_1}{\partial x_1}, \frac{\partial v_2}{\partial x_2}, \frac{\partial v_3}{\partial x_3}, \frac{\partial v_2}{\partial x_3}, \frac{\partial v_3}{\partial x_2}, \frac{\partial v_1}{\partial x_3}, \frac{\partial v_3}{\partial x_1}, \frac{\partial v_1}{\partial x_2}$, and $\frac{\partial v_2}{\partial x_1}$ and substitute in (28), which yields

$$\begin{aligned} \frac{\partial a_1}{\partial t} &= -w_1(a_1 + z_1) - w_2(a_2 + z_2) - 2w_3(a_3 + z_3) \\ \frac{\partial a_2}{\partial t} &= w_4(a_1 + z_1) + w_5(a_2 + z_2) + 2w_6(a_3 + z_3) \\ \frac{\partial a_3}{\partial t} &= w_7(a_1 + z_1) + w_8(a_2 + z_2) + 2w_9(a_3 + z_3) \\ \frac{\partial a_4}{\partial t} &= T_2(a_4 + z_4) - \frac{(a_4 + z_4)}{\tau_\sigma^{(2)}} \\ \frac{\partial a_5}{\partial t} &= T_3(a_5 + z_5) - \frac{(a_5 + z_5)}{\tau_\sigma^{(3)}} \\ \frac{\partial a_6}{\partial t} &= T_4(a_6 + z_6) - \frac{(a_6 + z_6)}{\tau_\sigma^{(4)}}, \end{aligned} \tag{30}$$

where

$$\begin{aligned} a_1 &= e_1 - z_1, & a_2 &= e_2 - z_2, & a_3 &= e_3 - z_3, \\ a_4 &= e_4 - z_4, & a_5 &= e_5 - z_5, & a_6 &= e_6 - z_6, \end{aligned}$$

and

$$d_1 = r_{11} + r_{12} + r_{13}, \quad d_2 = r_{33} + 2r_{13},$$

with r_{ij} being the elements of the inverse of unrelaxed compliance matrix

$$\mathbf{C}_p(\mathbf{x}) = \begin{bmatrix} c_{11}(\mathbf{x}) & c_{12}(\mathbf{x}) & c_{13}(\mathbf{x}) & 0 & 0 & 0 \\ c_{12}(\mathbf{x}) & c_{22}(\mathbf{x}) & c_{13}(\mathbf{x}) & 0 & 0 & 0 \\ c_{13}(\mathbf{x}) & c_{13}(\mathbf{x}) & c_{33}(\mathbf{x}) & 0 & 0 & 0 \\ 0 & 0 & 0 & c_{44}(\mathbf{x}) & 0 & 0 \\ 0 & 0 & 0 & 0 & c_{55}(\mathbf{x}) & 0 \\ 0 & 0 & 0 & 0 & 0 & c_{66}(\mathbf{x}) \end{bmatrix},$$

and inverse \mathbf{C}_p is given in [Appendix A](#).

$$\begin{aligned} z_1 &= T_1(d_1(\sigma_{11} + \sigma_{22}) + d_2\sigma_{33}), \\ z_2 &= T_2 \left[\left(r_{11} - \frac{1}{3}d_1 \right) \sigma_{11} + \left(r_{12} - \frac{1}{3}d_1 \right) \sigma_{22} + \left(r_{13} - \frac{1}{3}d_2 \right) \sigma_{33} \right], \\ z_3 &= T_3 \left[\left(r_{12} - \frac{1}{3}d_1 \right) \sigma_{11} + \left(r_{11} - \frac{1}{3}d_1 \right) \sigma_{22} + \left(r_{13} - \frac{1}{3}d_2 \right) \sigma_{33} \right], \\ z_4 &= T_2 c_{44}^{-1} \sigma_{23}, \quad z_5 = T_3 c_{55}^{-1} \sigma_{13}, \quad z_6 = T_4 c_{66}^{-1} \sigma_{12}, \end{aligned}$$

and

$$\begin{aligned} w_1 &= \left(T_1 p_\lambda + \frac{1}{\tau_\sigma^{(1)}} \right), & w_2 &= T_1 p_{\mu_1}, & w_3 &= T_1 p_{\mu_2}, \\ w_4 &= \left(\frac{T_2 p_\lambda}{3} - \frac{1}{\tau_\sigma^{(2)}} - K(r_{11} + r_{12}) \right), & w_5 &= (T_2 p_{\mu_1} - G(r_{11} - r_{13})), & w_6 &= (T_2 p_{\mu_2} - G(r_{12} - r_{13})), \\ w_7 &= \left(\frac{T_3 p_\lambda}{3} - \frac{1}{\tau_\sigma^{(3)}} - K(r_{12} + r_{11}) \right), & w_8 &= (T_3 p_{\mu_1} - G(r_{12} - r_{13})), & w_9 &= (T_3 p_{\mu_2} - G(r_{11} - r_{13})), \end{aligned}$$

with

$$p_\lambda = K(2d_1 + d_2), \quad p_{\mu_1} = G(d_1 - 2d_2), \quad p_{\mu_2} = 2G(d_1 - d_2).$$

We rewrite the system of equations (28) with out spatial derivative using the set of equations in (27), which yields

$$\begin{aligned} \mathbf{Q}_s^{-1}(\mathbf{x}) \frac{\partial \boldsymbol{\sigma}}{\partial t} &= \sum_{i=1}^d \mathbf{A}_i \frac{\partial \mathbf{v}}{\partial \mathbf{x}_i} + \mathbf{S} \boldsymbol{\sigma}, \\ \rho \frac{\partial \mathbf{v}}{\partial t} &= \sum_{i=1}^d \mathbf{A}_i^T \frac{\partial \boldsymbol{\sigma}}{\partial \mathbf{x}_i} + \mathbf{f}, \end{aligned} \tag{31}$$

where, $\boldsymbol{\sigma} = [\sigma_{11}, \sigma_{22}, \sigma_{33}, \sigma_{23}, \sigma_{13}, \sigma_{12}, a_1, a_2, a_3, a_4, a_5, a_6]^T$, and $\mathbf{v} = [v_1, v_2, v_3]^T$ and

$$\mathbf{Q}_s^{-1}(\mathbf{x}) = \left[\begin{array}{c|c} \mathbf{C}_p^{-1}(\mathbf{x}) & \mathbf{0} \\ \hline \mathbf{0} & \mathbf{I} \end{array} \right].$$

The matrices \mathbf{A}_i and \mathbf{S} are

$$\mathbf{A}_1 = \begin{bmatrix} 1 & 0 & 0 \\ 0 & 0 & 0 \\ 0 & 0 & 0 \\ 0 & 0 & 0 \\ 0 & 0 & 1 \\ 0 & 1 & 0 \\ 0 & 0 & 0 \\ 0 & 0 & 0 \\ 0 & 0 & 0 \\ 0 & 0 & 0 \\ 0 & 0 & 0 \\ 0 & 0 & 0 \end{bmatrix}, \quad \mathbf{A}_2 = \begin{bmatrix} 0 & 0 & 0 \\ 0 & 1 & 0 \\ 0 & 0 & 0 \\ 0 & 0 & 1 \\ 0 & 0 & 0 \\ 0 & 0 & 0 \\ 1 & 0 & 0 \\ 0 & 0 & 0 \\ 0 & 0 & 0 \\ 0 & 0 & 0 \\ 0 & 0 & 0 \\ 0 & 0 & 0 \end{bmatrix}, \quad \mathbf{A}_3 = \begin{bmatrix} 0 & 0 & 0 \\ 0 & 0 & 0 \\ 0 & 0 & 1 \\ 0 & 1 & 0 \\ 1 & 0 & 0 \\ 0 & 0 & 0 \\ 0 & 0 & 0 \\ 0 & 0 & 0 \\ 0 & 0 & 0 \\ 0 & 0 & 0 \\ 0 & 0 & 0 \\ 0 & 0 & 0 \end{bmatrix},$$

and $\mathbf{S} = \mathbf{Q}_s^{-1} \mathbf{G}$ with

$$\mathbf{G} = \left[\begin{array}{c|c} \mathbf{g}_{11 \times 6} & \mathbf{g}_{12 \times 6} \\ \hline \mathbf{g}_{21 \times 6} & \mathbf{g}_{22 \times 6} \end{array} \right]$$

where

$$\mathbf{g}_{11} = \begin{bmatrix} T_1 d_1 + 2GT_2 g_1 & KT_1 d_1 + 2GT_2 g_2 & KT_1 d_2 + 2GT_2 g_3 & 0 & 0 & 0 \\ KT_1 d_1 + 2GT_3 g_4 & KT_1 d_1 + 2GT_3 g_5 & KT_1 d_2 + 2GT_3 g_6 & 0 & 0 & 0 \\ KT_1 d_1 - 2Gg_7 & KT_1 d_1 - 2Gg_8 & KT_1 d_2 - 2Gg_9 & 0 & 0 & 0 \\ 0 & 0 & 0 & T_2 c_{44}^{-1} & 0 & 0 \\ 0 & 0 & 0 & 0 & T_3 c_{55}^{-1} & 0 \\ 0 & 0 & 0 & 0 & 0 & T_4 c_{66}^{-1} \end{bmatrix},$$

$$\mathbf{g}_{12} = \begin{bmatrix} K & 2G & 0 & 0 & 0 & 0 \\ K & 0 & 2G & 0 & 0 & 0 \\ K & -2G & -2G & 0 & 0 & 0 \\ 0 & 0 & 0 & c_{44} & 0 & 0 \\ 0 & 0 & 0 & 0 & c_{55} & 0 \\ 0 & 0 & 0 & 0 & 0 & c_{66} \end{bmatrix},$$

$$\mathbf{g}_{21} = \begin{bmatrix} t_1 & t_2 & t_3 & 0 & 0 & 0 \\ t_4 & t_5 & t_6 & 0 & 0 & 0 \\ t_7 & t_8 & t_9 & 0 & 0 & 0 \\ 0 & 0 & 0 & \left(T_2 - \frac{1}{\tau_\sigma^{(2)}}\right) T_2 / c_{44} & 0 & 0 \\ 0 & 0 & 0 & 0 & \left(T_3 - \frac{1}{\tau_\sigma^{(3)}}\right) T_3 / c_{55} & 0 \\ 0 & 0 & 0 & 0 & 0 & \left(T_4 - \frac{1}{\tau_\sigma^{(4)}}\right) T_4 / c_{66} \end{bmatrix},$$

$$\mathbf{g}_{22} = \begin{bmatrix} -w_1 & -w_2 & w_3 & 0 & 0 & 0 \\ w_4 & w_5 & w_6 & 0 & 0 & 0 \\ w_7 & w_8 & w_9 & 0 & 0 & 0 \\ 0 & 0 & 0 & \left(T_2 - \frac{1}{\tau_{\sigma}^{(2)}}\right) & 0 & 0 \\ 0 & 0 & 0 & 0 & \left(T_3 - \frac{1}{\tau_{\sigma}^{(3)}}\right) & 0 \\ 0 & 0 & 0 & 0 & 0 & \left(T_4 - \frac{1}{\tau_{\sigma}^{(4)}}\right) \end{bmatrix}$$

where

$$\begin{aligned} g_1 &= \left(r_{11} - \frac{1}{3}d_1\right), & g_2 &= \left(r_{12} - \frac{1}{3}d_1\right), & g_3 &= \left(r_{13} - \frac{1}{3}d_2\right), \\ g_4 &= \left(r_{12} - \frac{1}{3}d_1\right), & g_5 &= \left(r_{11} - \frac{1}{3}d_1\right), & g_6 &= \left(r_{13} - \frac{1}{3}d_2\right), \\ g_7 &= T_2g_1 + T_3g_4, & g_8 &= T_2g_2 + T_3g_5, & g_9 &= T_2g_3 + T_3g_6, \\ t_1 &= -(w_1T_1d_1 + w_2T_2g_1 + 2w_3T_3g_4), & t_2 &= -(w_1T_1d_1 + w_2T_2g_2 + 2w_3g_5), \\ t_3 &= -(w_1T_1d_2 + w_2T_2g_3 + 2w_3g_6), & t_4 &= w_4T_1d_1 + w_5T_2g_1 + 2w_6T_3g_4, \\ t_5 &= w_4T_1d_1 + w_5T_2g_2 + 2w_6g_5, & t_6 &= w_4T_1d_2 + w_5T_2g_3 + 2w_6g_6, \\ t_7 &= w_7T_1d_1 + w_8T_2g_1 + 2w_9T_3g_4, & t_8 &= w_7T_1d_1 + w_8T_2g_2 + 2w_9g_5, \\ t_9 &= w_7T_1d_2 + w_8T_2g_3 + 2w_9g_6. \end{aligned}$$

Here elements of \mathbf{G} and \mathbf{g}_{ij} are space dependent.

It should be noted that the matrices \mathbf{A}_i are spatially constant, while \mathbf{Q}_s^{-1} and ρ can vary spatially. We will also assume that ρ , \mathbf{Q}_s^{-1} and \mathbf{Q}_s^{-1} are positive-definite and bounded pointwise such that

$$\begin{aligned} 0 &< \rho_{\min} \leq \rho(\mathbf{x}) \leq \rho_{\max} < \infty \\ 0 &< c_{\min} \leq \mathbf{u}^T \mathbf{Q}_s(\mathbf{x}) \mathbf{u} \leq c_{\max} < \infty \\ 0 &< \hat{c}_{\min} \leq \mathbf{u}^T \mathbf{Q}_s^{-1}(\mathbf{x}) \mathbf{u} \leq \hat{c}_{\max} < \infty \end{aligned}$$

for all $\mathbf{x} \in \mathbb{R}^d$ and $\forall \mathbf{u} \in \mathbb{R}^{N_d}$.

Moreover, we assume that \mathbf{S} is a semi negative-definite and bounded pointwise such that

$$-\infty < s_{\min} \leq \mathbf{s}^T \mathbf{S} \mathbf{s} \leq s_{\max} < 0 \quad \forall \mathbf{x} \in \mathbb{R}^d \text{ and } \forall \mathbf{u} \in \mathbb{R}^{N_d}.$$

3. An energy stable discontinuous Galerkin formulation for the viscoelastic wave equation

Energy stable discontinuous Galerkin methods for viscoelastic wave propagation have been constructed based on the formulations of the system shown in (31). We assume that the domain Ω is exactly triangulated by a mesh Ω_h which consists of elements D^k which are images of a reference element \hat{D} under a local affine mapping.

$$\mathbf{x}^k = \Phi^k \hat{\mathbf{x}}.$$

Here $\mathbf{x}^k = \{x^k, y^k\}$ for $d = 2$ and $\mathbf{x}^k = \{x^k, y^k, z^k\}$ for $d = 3$ denote the physical coordinates on D^k and $\hat{\mathbf{x}} = \{\hat{x}, \hat{y}\}$ for $d = 2$ and $\hat{\mathbf{x}} = \{\hat{x}, \hat{y}, \hat{z}\}$ for $d = 3$ denote coordinates on the reference element. We denote the determinant of the Jacobian of Φ^k as J .

Solutions over each element D^k are approximated from a local space $V_h(D^k)$, which is defined as composition of the mapping Φ^k and the reference approximation space $V_h(\hat{D})$

$$V_h(D^k) = V_h(\hat{D}) \circ (\Phi^k)^{-1}.$$

Subsequently, the global approximation space $V_h(\Omega_h)$ is defined as

$$V_h(\Omega_h) = \bigoplus_k V_h(D^k).$$

In this work, we will take $V_h(\hat{D}) = P^N(\hat{D})$, with $P^N(\hat{D})$ being the space of polynomials of total degree N on the reference simplex. In two dimensions, P^N on a triangle is

$$P^N(\hat{D}) = \{\hat{x}^i \hat{y}^j, 0 \leq i + j \leq N\},$$

and in three dimensions, P^N on a tetrahedron is

$$P^N(\hat{D}) = \{\hat{x}^i \hat{y}^j \hat{x}^k, 0 \leq i + j + k \leq N\}.$$

The L^2 inner product and norm over D^k is represented as

$$(\mathbf{g}, \mathbf{h}) = \int_{D^k} \mathbf{g} \cdot \mathbf{h} \, d\mathbf{x} = \int_{\hat{D}} (\mathbf{g} \circ \Phi^k) \cdot (\mathbf{h} \circ \Phi^k) J \, d\hat{\mathbf{x}}, \quad \|\mathbf{g}\|_{L^2(\Omega)}^2 = (\mathbf{g}, \mathbf{g})_{L^2(D^k)},$$

where \mathbf{g} and \mathbf{h} are real vector-valued functions. Global L^2 inner products and squared norms are defined as the sum of local L^2 inner products and squared norms over each elements. The L^2 inner product and norm over the boundary ∂D^k of an element are similarly defined as

$$\langle \mathbf{u}, \mathbf{v} \rangle_{L^2(\partial D^k)} = \int_{\partial D^k} \mathbf{u} \cdot \mathbf{v} \, d\mathbf{x} = \sum_{f \in \partial D^k} \int_{\hat{f}} \mathbf{u} \cdot \mathbf{v} J^f \, d\hat{\mathbf{x}}, \quad \|\mathbf{u}\|_{L^2(\partial D^k)}^2 = \langle \mathbf{u}, \mathbf{u} \rangle,$$

where J^f is the Jacobian of the mapping from a reference face \hat{f} to a physical face f of an element.

Let f be a face of an element D^k with neighboring element $D^{k,+}$ and unit outward normal \mathbf{n} . Let u be a function with discontinuities across element interfaces. We define the interior value u^- and exterior value u^+ on face f of D^k

$$u^- = u|_{f \cap \partial D^k}, \quad u^+ = u|_{f \cap \partial D^{k,+}}.$$

The jump and average of a scalar function $u \in V_h(\Omega_h)$ over f are then defined as

$$[[u]] = u^+ - u^-, \quad \{ \{ u \} \} = \frac{u^+ + u^-}{2}.$$

Jumps and averages of vector-valued functions $\mathbf{u} \in \mathbb{R}^m$ and matrix-valued functions $\tilde{\mathbf{S}} \in \mathbb{R}^{m \times n}$ are defined component-wise.

$$([[\mathbf{u}]])_i = [[u_i]], \quad 1 \leq i \leq m \quad \left([[\tilde{\mathbf{S}}]] \right)_{ij} = [[\tilde{\mathbf{S}}]]_{ij}$$

We can now specify a DG formulation for the viscoelastic wave equation (31) which readily admits a DG formulation based on a penalty flux [33]. For the first order viscoelastic wave equation in (31), the DG formulation in strong form expressed as

$$\begin{aligned} \sum_{D^k \in \Omega_h} \left(\mathbf{Q}_s^{-1} \frac{\partial \boldsymbol{\sigma}}{\partial t}, \mathbf{h} \right)_{L^2(D^k)} &= \sum_{D^k \in \Omega_h} \left(\left(\sum_{i=1}^d \mathbf{A}_i \frac{\partial \mathbf{v}}{\partial \mathbf{x}_i}, \mathbf{h} \right)_{L^2(D^k)} + \left\langle \frac{1}{2} \mathbf{A}_n [[\mathbf{v}]] + \frac{\alpha_{\boldsymbol{\sigma}}}{2} \mathbf{A}_n \mathbf{A}_n^T [[\boldsymbol{\sigma}]], \mathbf{h} \right\rangle_{L^2(\partial D^k)} \right. \\ &\quad \left. + (\mathbf{S} \boldsymbol{\sigma}, \mathbf{g})_{L^2(D^k)} \right) \\ \sum_{D^k \in \Omega_h} \left(\rho \frac{\partial \mathbf{v}}{\partial t}, \mathbf{g} \right)_{L^2(D^k)} &= \sum_{D^k \in \Omega_h} \left(\left(\sum_{i=1}^d \mathbf{A}_i^T \frac{\partial \boldsymbol{\sigma}}{\partial \mathbf{x}_i} + \mathbf{f}, \mathbf{g} \right)_{L^2(D^k)} + \left\langle \frac{1}{2} \mathbf{A}_n^T [[\boldsymbol{\sigma}]] + \frac{\alpha_{\mathbf{v}}}{2} \mathbf{A}_n^T \mathbf{A}_n [[\mathbf{v}]], \mathbf{g} \right\rangle_{L^2(\partial D^k)} \right), \end{aligned} \quad (32)$$

for all $\mathbf{h}, \mathbf{g} \in V_h(\Omega_h)$. Here, \mathbf{A}_n is the normal matrix defined on a face f of an element

$$\mathbf{A}_n = \sum_{i=1}^d n_i \mathbf{A}_i = \begin{bmatrix} n_x & 0 & 0 \\ 0 & n_y & 0 \\ 0 & 0 & n_z \\ 0 & n_z & n_y \\ n_z & 0 & n_x \\ n_y & n_x & 0 \\ 0 & 0 & 0 \\ 0 & 0 & 0 \\ 0 & 0 & 0 \\ 0 & 0 & 0 \\ 0 & 0 & 0 \\ 0 & 0 & 0 \end{bmatrix}.$$

The factors α_τ, α_v are penalty parameters and defined on element interfaces. We assume that α_τ and $\alpha_v \geq 0$ and are piecewise constant over each shared face between two elements. These penalty constants can be taken to be zero, which results in a non-dissipative central flux, while $\alpha_\tau, \alpha_v > 0$ results in energy dissipation similar to the upwind flux [24, 34, 35]. The stability of DG formulations are independent of the magnitude of these penalty parameters. However, a naive choice of these parameters can result in a stiffer semi-discrete system of ODEs and necessitates a smaller time under explicit time integration schemes [34, 35]. In this work, we take $\alpha = 1/2$ unless stated otherwise.

In most of DG formulations, material parameters are present in the numerical flux and in the penalty parameters α . However, for the presented formulation, the scheme is stable and high order accurate even when the penalty parameters are zero. The difference in the presented formulation is that the material data has been factored out into the mass matrix multiplying the time derivative. Multiplying by the inverse mass matrix incorporates material parameters through an appropriate combination and scaling of the flux terms [34].

3.1. Boundary Conditions

In many applications, the top surface of a domain is a free surface boundary (stress free), with remaining surfaces taken to be absorbing boundaries. In our DG formulation, the boundary conditions are imposed by choosing appropriate exterior values which result in modified boundary numerical fluxes. Boundary conditions on the normal components of the stress can be imposed by modifying the term $[\![\mathbf{A}_n^T \boldsymbol{\tau}]\!] = [\![\tilde{\mathbf{S}} \mathbf{n}]\!]$ in numerical flux, where $\tilde{\mathbf{S}}$ is

$$\tilde{\mathbf{S}} = \begin{bmatrix} \sigma_{11} & \sigma_{12} & \sigma_{13} \\ \sigma_{12} & \sigma_{22} & \sigma_{23} \\ \sigma_{13} & \sigma_{23} & \sigma_{33} \end{bmatrix}.$$

For a face of the element lying on the top surface of the domain, free surface boundary or zero traction conditions can be imposed by setting

$$[\![\mathbf{A}_n^T \boldsymbol{\sigma}]\!] = [\![\tilde{\mathbf{S}} \mathbf{n}]\!] = -2\tilde{\mathbf{S}}^- \mathbf{n} = -2\mathbf{A}_n^T \boldsymbol{\sigma}^-, \quad \mathbf{v}^+ = \mathbf{v}^- \implies [\![\mathbf{v}]\!] = 0.$$

For problems which require the truncation of infinite or large domains, basic “extrapolation” absorbing boundary conditions can be imposed by setting

$$[\![\mathbf{A}_n^T \boldsymbol{\sigma}]\!] = [\![\tilde{\mathbf{S}} \mathbf{n}]\!] = -\tilde{\mathbf{S}}^- \mathbf{n} = -\mathbf{A}_n^T \boldsymbol{\sigma}^-, \quad \mathbf{v}^+ = 0 \implies [\![\mathbf{v}]\!] = -\mathbf{v}^-.$$

In addition to the above boundary conditions, more accurate absorbing boundary conditions can be also imposed using perfectly matching layers (PML) [36] or high order absorbing boundary conditions (HABC) [37]. However, in all cases, the boundary conditions are imposed by computing the numerical fluxes based on the modified jumps, ensuring energy stability for free surface and absorbing boundary conditions.

3.2. Energy stability

The DG formulation in (32) can be proven to be energy stable in the absence of external forces ($\mathbf{f} = 0$) and for free-surface and absorbing boundary conditions. Integrating by parts the velocity equation in (32) gives

$$\begin{aligned} \sum_{D^k \in \Omega_h} \left(\mathbf{Q}_s^{-1} \frac{\partial \boldsymbol{\sigma}}{\partial t}, \mathbf{h} \right)_{L^2(D^k)} &= \sum_{D^k \in \Omega_h} \left(\left(\sum_{i=1}^d \mathbf{A}_i \frac{\partial \mathbf{v}}{\partial \mathbf{x}_i}, \mathbf{h} \right)_{L^2(D^k)} + \left\langle \frac{1}{2} \mathbf{A}_n \llbracket \mathbf{v} \rrbracket + \frac{\alpha_{\boldsymbol{\sigma}}}{2} \mathbf{A}_n \mathbf{A}_n^T \llbracket \boldsymbol{\sigma} \rrbracket, \mathbf{h} \right\rangle_{L^2(\partial D^k)} \right. \\ &\quad \left. + (\mathbf{S} \boldsymbol{\sigma}, \boldsymbol{\sigma})_{L^2(D^k)} \right) \\ \sum_{D^k \in \Omega_h} \left(\rho \frac{\partial \mathbf{v}}{\partial t}, \mathbf{g} \right)_{L^2(D^k)} &= \sum_{D^k \in \Omega_h} \left(- \left(\sum_{i=1}^d \boldsymbol{\sigma}, \mathbf{A}_i \frac{\partial \mathbf{g}}{\partial \mathbf{x}_i} \right)_{L^2(D^k)} \right. \\ &\quad \left. + \left\langle \mathbf{A}_n^T \{ \boldsymbol{\sigma} \} + \frac{\alpha_{\mathbf{v}}}{2} \mathbf{A}_n^T \mathbf{A}_n \llbracket \mathbf{v} \rrbracket, \mathbf{g} \right\rangle_{L^2(\partial D^k)} \right) \end{aligned} \quad (33)$$

Taking $(\mathbf{h}, \mathbf{g}) = (\boldsymbol{\sigma}, \mathbf{v})$ in (33) and adding both equations together yields

$$\begin{aligned} \sum_{D^k \in \Omega_h} \frac{1}{2} \frac{\partial}{\partial t} ((\mathbf{Q}_s^{-1} \boldsymbol{\sigma}, \boldsymbol{\sigma})_{L^2(D^k)} + (\rho \mathbf{v}, \mathbf{v})_{L^2(D^k)}) \\ &= \sum_{D^k \in \Omega_h} \left\langle \frac{1}{2} \mathbf{A}_n \llbracket \mathbf{v} \rrbracket + \frac{\alpha_{\boldsymbol{\sigma}}}{2} \mathbf{A}_n \mathbf{A}_n^T \llbracket \boldsymbol{\sigma} \rrbracket, \mathbf{h} \right\rangle_{L^2(\partial D^k)} + \left\langle \mathbf{A}_n^T \{ \boldsymbol{\sigma} \} + \frac{\alpha_{\mathbf{v}}}{2} \mathbf{A}_n^T \mathbf{A}_n \llbracket \mathbf{v} \rrbracket, \mathbf{g} \right\rangle_{L^2(\partial D^k)} \\ &\quad + (\mathbf{S} \boldsymbol{\sigma}, \boldsymbol{\sigma})_{L^2(D^k)} \\ &= \sum_{D^k \in \Omega_h} \sum_{f \in \partial D^k} \int_f \left(\frac{1}{2} \boldsymbol{\sigma}^T \mathbf{A}_n \llbracket \mathbf{v} \rrbracket + \frac{\alpha_{\boldsymbol{\sigma}}}{2} \boldsymbol{\sigma}^T \mathbf{A}_n \mathbf{A}_n^T \llbracket \boldsymbol{\sigma} \rrbracket + \mathbf{v}^T \mathbf{A}_n^T \{ \boldsymbol{\sigma} \} + \frac{\alpha_{\mathbf{v}}}{2} \mathbf{v}^T \mathbf{A}_n^T \mathbf{A}_n \llbracket \mathbf{v} \rrbracket \right) d\mathbf{x} \\ &\quad + \sum_{D^k \in \Omega_h} \int_{D^k} \boldsymbol{\sigma}^T \mathbf{S} \boldsymbol{\sigma} d\mathbf{x}, \end{aligned}$$

where the term

$$\sum_{D^k \in \Omega_h} \frac{1}{2} \frac{\partial}{\partial t} ((\mathbf{Q}_s^{-1} \boldsymbol{\sigma}, \boldsymbol{\sigma})_{L^2(D^k)} + (\rho \mathbf{v}, \mathbf{v})_{L^2(D^k)})$$

is the total energy of the system.

Let Γ_h be the set of unique faces in Ω_h and let $\Gamma_{\boldsymbol{\sigma}}$, Γ_{abc} denote boundaries where free-surface and absorbing boundary conditions are imposed, respectively. We split surface terms into contributions from interior shared faces and from boundary faces. On interior shared faces, we sum the contributions from the two adjacent elements, which gives

$$\begin{aligned} \sum_{f \in \Gamma_h \setminus \partial \Omega} \int_f \left(\frac{1}{2} \boldsymbol{\tau}^T \mathbf{A}_n \llbracket \mathbf{v} \rrbracket + \frac{\alpha_{\boldsymbol{\sigma}}}{2} \boldsymbol{\sigma}^T \mathbf{A}_n \mathbf{A}_n^T \llbracket \boldsymbol{\sigma} \rrbracket + \mathbf{v}^T \mathbf{A}_n^T \{ \boldsymbol{\sigma} \} + \frac{\alpha_{\mathbf{v}}}{2} \mathbf{v}^T \mathbf{A}_n^T \mathbf{A}_n \llbracket \mathbf{v} \rrbracket \right) d\mathbf{x} + \sum_{D^k \in \Omega_h} \int_{D^k} \boldsymbol{\sigma}^T \mathbf{D} \boldsymbol{\sigma} d\mathbf{x} \\ = - \sum_{f \in \Gamma_h \setminus \partial \Omega} \int_f \left(\frac{\alpha_{\boldsymbol{\sigma}}}{2} |\mathbf{A}_n^T \llbracket \boldsymbol{\sigma} \rrbracket|^2 + \frac{\alpha_{\mathbf{v}}}{2} |\mathbf{A}_n \llbracket \mathbf{v} \rrbracket|^2 \right) d\mathbf{x} + \sum_{D^k \in \Omega_h} \int_{D^k} \mathbf{v}^T \mathbf{S} \mathbf{v} d\mathbf{x}, \end{aligned}$$

where $\mathbf{v}^T \mathbf{S} \mathbf{v} < 0$, since \mathbf{S} is a negative semi-definite matrix. For faces which lie on $\Gamma_{\boldsymbol{\sigma}}$, $\mathbf{A}_n^T = -2\mathbf{A}_n^T \boldsymbol{\sigma}^-$, $\mathbf{A}_n^T \{ \boldsymbol{\sigma} \} =$

0 and $\llbracket \mathbf{v} \rrbracket = 0$ yielding

$$\begin{aligned} & \sum_{f \in \Gamma_\sigma} \int_f \left(\frac{1}{2} \boldsymbol{\sigma}^T \mathbf{A}_n \llbracket \mathbf{v} \rrbracket + \frac{\alpha_\sigma}{2} \boldsymbol{\sigma}^T \mathbf{A}_n \mathbf{A}_n^T \llbracket \boldsymbol{\tau} \rrbracket + \mathbf{v}^T \mathbf{A}_n^T \{ \{ \boldsymbol{\sigma} \} \} + \frac{\alpha_v}{2} \mathbf{v}^T \mathbf{A}_n^T \mathbf{A}_n \llbracket \mathbf{v} \rrbracket \right) d\mathbf{x} \\ &= - \sum_{f \in \Gamma_\tau} \int_f \left(\alpha_\sigma |\mathbf{A}_n^T \boldsymbol{\sigma}^-|^2 \right) d\mathbf{x}. \end{aligned}$$

Finally, for faces in Γ_{abc} , we have $\mathbf{A}_n^T \{ \{ \boldsymbol{\sigma} \} \} = \frac{1}{2} \mathbf{A}_n^T \boldsymbol{\sigma}^-$, $\mathbf{A}_n^T \llbracket \boldsymbol{\sigma} \rrbracket = -\mathbf{A}_n^T \boldsymbol{\sigma}^-$ and $\llbracket \mathbf{v} \rrbracket = -\mathbf{v}^-$, yielding

$$\begin{aligned} & \sum_{f \in \Gamma_h \setminus \partial\Omega} \int_f \left(\frac{1}{2} \boldsymbol{\sigma}^T \mathbf{A}_n \llbracket \mathbf{v} \rrbracket + \frac{\alpha_\sigma}{2} \boldsymbol{\sigma}^T \mathbf{A}_n \mathbf{A}_n^T \llbracket \boldsymbol{\sigma} \rrbracket + \mathbf{v}^T \mathbf{A}_n^T \{ \{ \boldsymbol{\sigma} \} \} + \frac{\alpha_v}{2} \mathbf{v}^T \mathbf{A}_n^T \mathbf{A}_n \llbracket \mathbf{v} \rrbracket \right) d\mathbf{x} \\ &= - \sum_{f \in \Gamma_{\text{abc}}} \int_f \left(\frac{\alpha_\sigma}{2} |\mathbf{A}_n^T \boldsymbol{\sigma}^-|^2 + \frac{\alpha_v}{2} |\mathbf{A}_n \mathbf{v}^-|^2 \right) d\mathbf{x}, \end{aligned}$$

Combining contributions from all faces and dissipation in the system yields the following result:

Theorem 1. *The DG formulation in (32) is energy stable for $\alpha_\sigma, \alpha_v \geq 0$ such that*

$$\begin{aligned} & \sum_{D^k \in \Omega_h} \frac{1}{2} \frac{\partial}{\partial t} ((\mathbf{Q}_s^{-1} \boldsymbol{\sigma}, \boldsymbol{\sigma})_{L^2(D^k)} + (\rho \mathbf{v}, \mathbf{v})_{L^2(D^k)}) = - \sum_{f \in \Gamma_h \setminus \partial\Omega} \int_f \left(\frac{\alpha_\sigma}{2} |\mathbf{A}_n^T \llbracket \boldsymbol{\sigma} \rrbracket|^2 + \frac{\alpha_v}{2} |\mathbf{A}_n \llbracket \mathbf{v} \rrbracket|^2 \right) d\mathbf{x} \\ & - \sum_{f \in \Gamma_\sigma} \int_f \left(\alpha_\sigma |\mathbf{A}_n^T \boldsymbol{\sigma}^-|^2 \right) d\mathbf{x} - \sum_{f \in \Gamma_{\text{abc}}} \int_f \left(\frac{\alpha_\sigma}{2} |\mathbf{A}_n^T \boldsymbol{\sigma}^-|^2 + \frac{\alpha_v}{2} |\mathbf{A}_n \mathbf{v}^-|^2 \right) d\mathbf{x} \\ & + \sum_{D^k \in \Omega_h} \int_{D^k} \mathbf{v}^T \mathbf{S} \mathbf{v} d\mathbf{x} \leq 0. \end{aligned} \tag{34}$$

The left hand side of (34) is an L^2 -equivalent norm on $(\boldsymbol{\tau}, \mathbf{v})$ as \mathbf{Q}_s^{-1} and ρ are positive definite. Theorem 1 implies that magnitude of the DG solution is non-increasing in time dissipation is present for penalization parameters $\alpha_\tau, \alpha_v \geq 0$.

3.3. The semi-discrete matrix system for DG

Let $\{\phi_i\}_{i=1}^{N_p}$ be a nodal basis function for $P^N(\widehat{D})$ located at Warp and Blend interpolation points [24]. These basis functions are defined implicitly using an orthogonal polynomial basis on the reference simplex. We define the reference mass matrix $\widehat{\mathbf{M}}$ and the physical mass matrix \mathbf{M} for an element D^k as

$$(\widehat{\mathbf{M}})_{ij} = \int_{\widehat{D}} \phi_j \phi_i d\widehat{\mathbf{x}}, \quad (\mathbf{M}_{ij}) = \int_{D^k} \phi_j \phi_i d\mathbf{x} = \int_{\widehat{D}} \phi_j \phi_i J d\widehat{\mathbf{x}}.$$

J is constant for affine mappings, and $\mathbf{M} = J \widehat{\mathbf{M}}$. We also define weak differentiation matrices \mathbf{S}_k and face mass matrices \mathbf{M}_f such that

$$(\mathbf{S}_k)_{ij} = \int_{D^k} \frac{\partial \phi_j}{\partial \mathbf{x}_k} \phi_i d\mathbf{x}, \quad (\mathbf{M}_f)_{ij} = \int_f \phi_j \phi_i d\mathbf{x} = \int_{\widehat{f}} \phi_j \phi_i J^f d\widehat{\mathbf{x}},$$

where J^f is the Jacobian of the mapping from the reference face \widehat{f} to f . For affinely mapped simplices, J^f is also constant and $M_f = J^f \widehat{\mathbf{M}}_f$, where the definition of the reference face mass matrix $\widehat{\mathbf{M}}_f$ is analogous to the definition of the reference mass matrix $\widehat{\mathbf{M}}$.

Finally, we introduce weighted mass matrices. Let $w(\mathbf{x}) \in \mathbb{R}$ and $\mathbf{W}(\mathbf{x}) \in \mathbb{R}^{m \times n}$. Then, scalar and matrix-weighted mass matrices \mathbf{M}_w and \mathbf{M}_W are defined as

$$(\mathbf{M}_w)_{ij} = \int_{D^k} w(\mathbf{x}) \phi_j(\mathbf{x}) \phi_i(\mathbf{x}) \, d\mathbf{x}, \quad \mathbf{M}_W = \begin{bmatrix} \mathbf{M}_{W_{1,1}} & \cdots & \mathbf{M}_{W_{1,n}} \\ \vdots & \ddots & \vdots \\ \mathbf{M}_{W_{m,1}} & \cdots & \mathbf{M}_{W_{m,n}} \end{bmatrix} \quad (35)$$

where $\mathbf{M}_{W_{i,j}}$ is the scalar weighted mass matrix weighted by the $(i, j)^{\text{th}}$ element of \mathbf{W} . Note that $\mathbf{M}_w, \mathbf{M}_W$ are positive definite if $w(x), \mathbf{W}$ are pointwise positive definite.

Local contributions to the DG variational form may be evaluated in a quadrature-free manner using matrix-weighted mass matrices as defined above. Let $\boldsymbol{\Sigma}_i, \mathbf{V}_i$ denote vectors containing degrees of freedom for solutions components $\boldsymbol{\sigma}_i$ and \mathbf{v}_i , such that

$$\begin{aligned} \mathbf{v}_i(\mathbf{x}, t) &= \sum_{j=1}^{N_p} (\mathbf{V}_i(t))_j \phi_j(\mathbf{x}), & 1 \leq i \leq 6 \\ \boldsymbol{\sigma}_i(\mathbf{x}, t) &= \sum_{j=1}^{N_p} (\boldsymbol{\Sigma}_i(t))_j \phi_j(\mathbf{x}), & 1 \leq i \leq 7 \end{aligned}$$

Then, the local DG formulation can be written as a block system of ordinary differential equations by concatenating $\boldsymbol{\Sigma}_i, \mathbf{V}_i$ into single vectors $\boldsymbol{\Sigma}$ and \mathbf{V} and using the Kronecker product \otimes

$$\mathbf{M}_{Q_s^{-1}} \frac{\partial \boldsymbol{\Sigma}}{\partial t} = \sum_{i=1}^d (\mathbf{A}_i \otimes \mathbf{S}_i) \mathbf{V} + \sum_{f \in \partial D^k} (\mathbf{I} \otimes \mathbf{M}_f) \mathbf{F}_\sigma + \mathbf{M}_S \boldsymbol{\Sigma} \quad (36)$$

$$\mathbf{M}_\rho \frac{\partial \mathbf{V}}{\partial t} = \sum_{i=1}^d (\mathbf{A}_i^T \otimes \mathbf{S}_i) \boldsymbol{\Sigma} + \sum_{f \in \partial D^k} (\mathbf{I} \otimes \mathbf{M}_f) \mathbf{F}_v, \quad (37)$$

where \mathbf{F}_v and \mathbf{F}_σ denote the degrees of freedom for the velocity and stress numerical fluxes.

In order to apply a time integrator, we must invert \mathbf{M}_{Q_s} and \mathbf{M}_ρ . While the inversion of $\mathbf{M}_{Q_s^{-1}}$ and \mathbf{M}_ρ can be parallelized from element to element, doing so typically requires either the precomputation and storage of the dense matrix inverses or on-the-fly construction and solution of a large dense matrix system at every time step. The former option requires a large amount of storage, while the latter option is computationally expensive and difficult to parallelize among degrees of freedom. This cost can be avoided when Q_s^{-1} and ρ are constant over an element D^k . In this case, \mathbf{M}_{Q_s} reduces to

$$\mathbf{M}_{Q_s^{-1}}^{-1} = \begin{bmatrix} Q_s^{-1}(1,1) \mathbf{M} & \cdots & Q_s^{-1}(1,N_d) \mathbf{M} \\ \vdots & \ddots & \vdots \\ Q_s^{-1}(N_d,1) \mathbf{M} & \cdots & Q_s^{-1}(N_d,N_d) \mathbf{M} \end{bmatrix}^{-1} = (Q_s \otimes \mathbf{M})^{-1} = Q_s \otimes \left(\frac{1}{J} \widehat{\mathbf{M}}^{-1} \right).$$

Similarly \mathbf{M}_S^{-1} and \mathbf{M}_ρ^{-1} can be expressed as $\mathbf{M}_S = \mathbf{S} \otimes \left(\frac{1}{J} \widehat{\mathbf{M}}^{-1} \right)$ and $\mathbf{M}_\rho^{-1} = \rho^{-1} \otimes \left(\frac{1}{J} \widehat{\mathbf{M}}^{-1} \right)$, and respectively. Applying these observations to (36) and (37) yields the following sets of local ODEs over each element

$$\frac{\partial \boldsymbol{\Sigma}}{\partial t} = \sum_{i=1}^d (Q_s \mathbf{A} \otimes D_i) \mathbf{V} + \sum_{f \in \partial D^k} (Q_s \otimes \mathbf{M}_f) \mathbf{F}_\sigma + \mathbf{M}_{Q_s^{-1}}^{-1} \mathbf{M}_D \boldsymbol{\Sigma}, \quad (38)$$

$$\frac{\partial \mathbf{V}}{\partial t} = \sum_{i=1}^d (\rho^{-1} \mathbf{A}^T \otimes D_i) \boldsymbol{\Sigma} + \sum_{f \in \partial D^k} (\rho^{-1} \otimes \mathbf{M}_f) \mathbf{F}_v \quad (39)$$

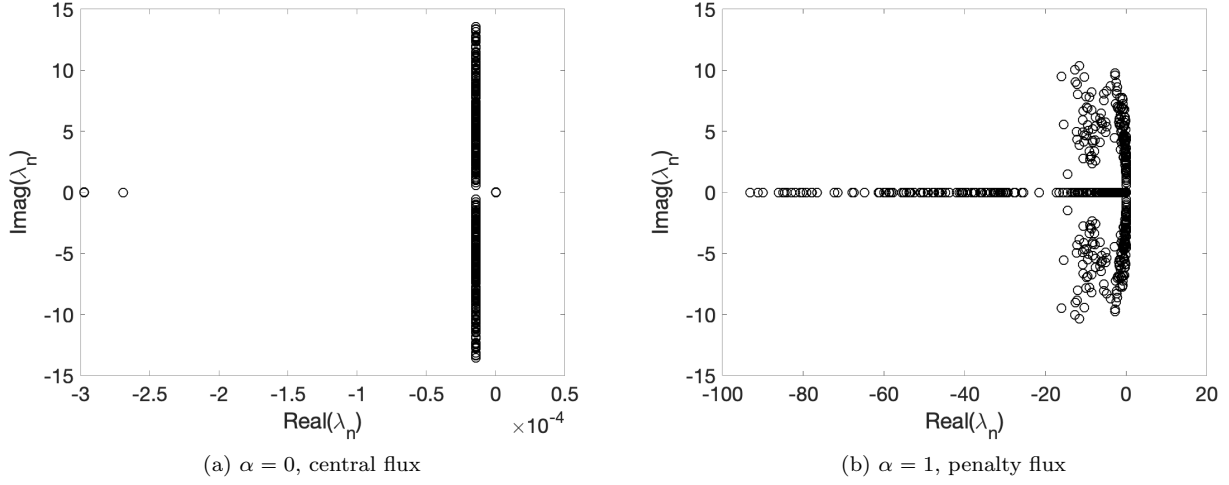


Figure 1: Spectra for $N = 3$ and $h = 1/2$ with a material property of isotropic Sandstone (Column 3 of Table 1). For $\alpha_\tau = \alpha_v = 0$ and $\alpha_\tau = \alpha_v = 1$, the largest real part of spectra are $1.83519e - 14$ and $2.18232e - 14$, respectively.

where we have introduced the differentiation matrix $\mathbf{D}_i = \mathbf{M}^{-1}\mathbf{S}_i$ and lift matrix $\mathbf{L}_f = \mathbf{M}^{-1}\mathbf{M}_f$. For affine elements, both derivative and lift matrices are applied using products of geometric factors and reference derivative and lift matrices.

If \mathbf{Q}_s^{-1} and ρ vary spatially within the element, then the above approach can no longer be used to invert \mathbf{Q}_s and \mathbf{Q}_v . This case can be treated using the approach of [33], where $\mathbf{M}_{\mathbf{Q}_s}, \rho$ are replaced with weight-adjusted approximations. These approximations are low storage, simple to invert, and yield an energy stable and high order accurate DG method to approximate the matrix-weighted L^2 inner product (and corresponding matrix-weighted mass-matrices \mathbf{Q}_s and ρ).

We also note that, material coefficients \mathbf{Q}_s^{-1} , ρ appear only on the left hand side of (31). The right hand side of (31) is equivalent to the discretization of a constant coefficient system. This provides additional advantages in that the right hand side can be evaluated using efficient techniques for DG discretizations of constant-coefficient problems [38, 39].

4. Numerical experiments

In this section, we present several numerical experiments to validate the stability and accuracy of the proposed method in two and three dimensions. The convergence of the new DG formulation in piecewise constant isotropic viscoelastic media is confirmed. Finally, the method is applied to solve the anisotropic viscoelastic wave equation in various heterogeneous media.

Time integration is performed using the low-storage 4th order five-stage Runge-Kutta scheme of Carpenter and Kennedy [40], and the time step is chosen based on the global estimate

$$dt = \min_k \frac{C_{CFL}}{\max(\lambda_i) C_N \|Jf\|_{L^\infty(\partial D^k)} \|J^{-1}\|_{L^\infty(D^k)}} \quad (40)$$

where λ_i are wave speeds of the system [23], $C_N = O(N^2)$ is the order-dependent constant in the surface polynomial trace inequality [41], and C_{CFL} is a tunable global CFL constant. This estimate is derived by bounding the eigenvalues of the spatial DG discretization matrix appearing in the semi-discrete system of ODEs. This choice of dt is very conservative as it is derived based on an upper bound on the spectral radius.

Table 1: Material properties of anisotropic-viscoelastic media [7]

Properties	Clay shale	Phenolic	Isotropic Sandstone
Elasticities			
ρ_s (kg/m ³)	2590	1364	2500
c_{11} (GPa)	66.6	11.7	25.6
c_{12} (GPa)	19.7	6.7	9.4
c_{13} (GPa)	39.4	7.0	9.4
c_{22} (GPa)	66.6	15.4	25.6
c_{23} (GPa)	39.4	7.0	9.4
c_{33} (GPa)	39.9	17.4	25.6
c_{44} (GPa)	10.9	3.8	16.2
c_{55} (GPa)	10.9	3.5	16.2
c_{66} (GPa)	23.4	3.1	16.2
Relaxation time (s)			
$\tau_\epsilon^{(1)}$	8.00×10^{-3}	6.4×10^{-3}	3.72×10^{-3}
$\tau_\sigma^{(1)}$	7.49×10^{-3}	6.00×10^{-3}	3.36×10^{-3}
$\tau_\epsilon^{(2)}$	8.00×10^{-3}	6.4×10^{-3}	3.78×10^{-3}
$\tau_\sigma^{(2)}$	7.25×10^{-3}	5.80×10^{-3}	3.30×10^{-3}
$\tau_\epsilon^{(3)}$	8.00×10^{-3}	6.4×10^{-3}	3.78×10^{-3}
$\tau_\sigma^{(3)}$	7.25×10^{-3}	5.60×10^{-3}	3.30×10^{-3}
$\tau_\epsilon^{(4)}$	8.00×10^{-3}	6.4×10^{-3}	3.78×10^{-3}
$\tau_\sigma^{(4)}$	7.25×10^{-3}	5.30×10^{-3}	3.30×10^{-3}

4.1. Spectra and choice of penalty parameter

We first verify the energy stability of proposed DG formulation. Let \mathbf{A}_h denote the matrix induced by the global semi-discrete DG formulation, such that time evolution of the solution \mathbf{q} is governed by

$$\frac{\partial \mathbf{q}}{\partial t} = \mathbf{A}_h \mathbf{q},$$

where \mathbf{q} denotes a vector of degrees of freedom. We show in Figure 1 eigenvalues of \mathbf{A}_h for $\alpha = 0$ and $\alpha = 1$ with material parameters of isotropic sandstone (given in Column 3 of Table 1). The discretization parameters are $N = 3$ and $h = 1/2$. In both cases, the largest real part of any eigenvalues is $O(10^{-14})$, which suggests that the semi-discrete scheme is indeed energy stable. It is to be also noted that some eigenvalues for $\alpha = 0$ have purely negative real part, corresponding to the dissipation present in viscoelastic system.

For practical simulations, the choice of the penalty parameter α remains to be specified. Taking $\alpha > 0$ results in damping of under-resolved spurious components of the solutions. However, a naive selection of α can result in an overly restrictive time-step restriction for stability. A guiding principle for determining appropriate values of the penalty parameters α is to ensure that the spectral radius is the same magnitude as the case when $\alpha = 0$. For example, the spectral radius of \mathbf{A}_h , $\rho(\mathbf{A}_h)$ is 13.5653 for $\alpha = 0$ which is $O(N^2/h)$. The spectral radius $\rho(\mathbf{A}_h)$ is 45.6388 for $\alpha_\tau, \alpha_v = 0.5$, while the spectral radius for $\alpha_\tau, \alpha_v = 1$ is $\rho(\mathbf{A}_h) = 93.1184$. Since the maximum stable time step is proportional to the spectral radius, taking $\alpha = 1$ in this case results in a more restrictive CFL condition. This phenomena is related to observations in [42] that large penalty parameters result in extremal eigenvalues of \mathbf{A}_h with very large negative real parts.

4.2. Convergence for a plane wave in viscoelastic medium

The analytical solution to (29) for a plane wave is given as

$$\mathbf{q}_n(\mathbf{x}, t) = \mathbf{q}_n^0 \exp[i \cdot (\omega t - \mathbf{k} \cdot \mathbf{x})], \quad n = 1 \dots 15, \quad (41)$$

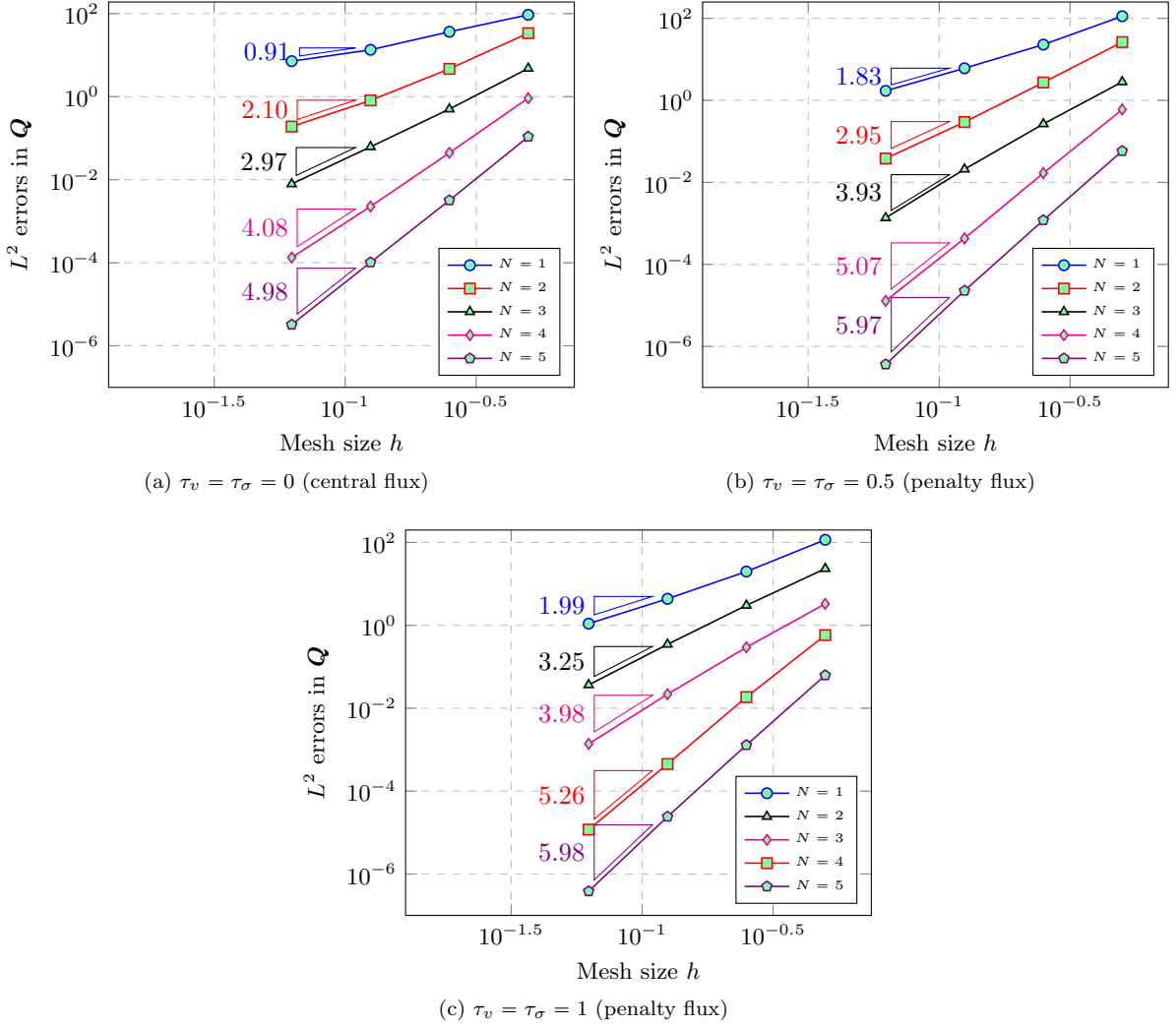


Figure 2: Convergence of L^2 error for plane wave in a viscoelastic media

where \mathbf{Q}_n^0 is the initial amplitude vector of stress and velocity components; ω are wave frequencies; $\mathbf{k} = (k_x, k_y, k_z)$ is the wave-number vector. To achieve realistic viscoelastic behavior, we superimpose three plane waves, of the form given by (41), corresponding to a P-wave, and S-wave.

Now, we briefly describe how we determine the wave frequencies ω . Substituting (41) into (29) yields

$$\omega \mathbf{q}_n^0 = (\mathbf{A}(\mathbf{x})k_x + \mathbf{B}(\mathbf{x})k_y + \mathbf{C}(\mathbf{x})k_z - i\mathbf{D}(\mathbf{x}))\mathbf{q}_n^0 \quad (42)$$

Solving the three eigenvalues problem for in (42) for each wave mode l yields in matrix of right eigenvectors $(R_{mn}^{(l)})$ and eigenvalue (ω_l) . Following [43, 44], the solution of (29) for the plane wave can be constructed as

$$\mathbf{q}_n(\mathbf{x}, t) = \sum_{l=1}^2 R_{mn}^{(l)} \gamma_n^{(l)} \exp[i \cdot (\omega^{(l)} t - \mathbf{k}^{(l)} \cdot \mathbf{x})], \quad (43)$$

where $\gamma_n^{(l)}$ is a amplitude coefficient with $\gamma_1^{(1)} = \gamma_2^{(2)} = 1$.

Next, we study the accuracy and convergence of our DG method for a plane wave propagating in an isotropic porous sandstone with material properties given in Table 1 (Column 3). Unless otherwise stated,

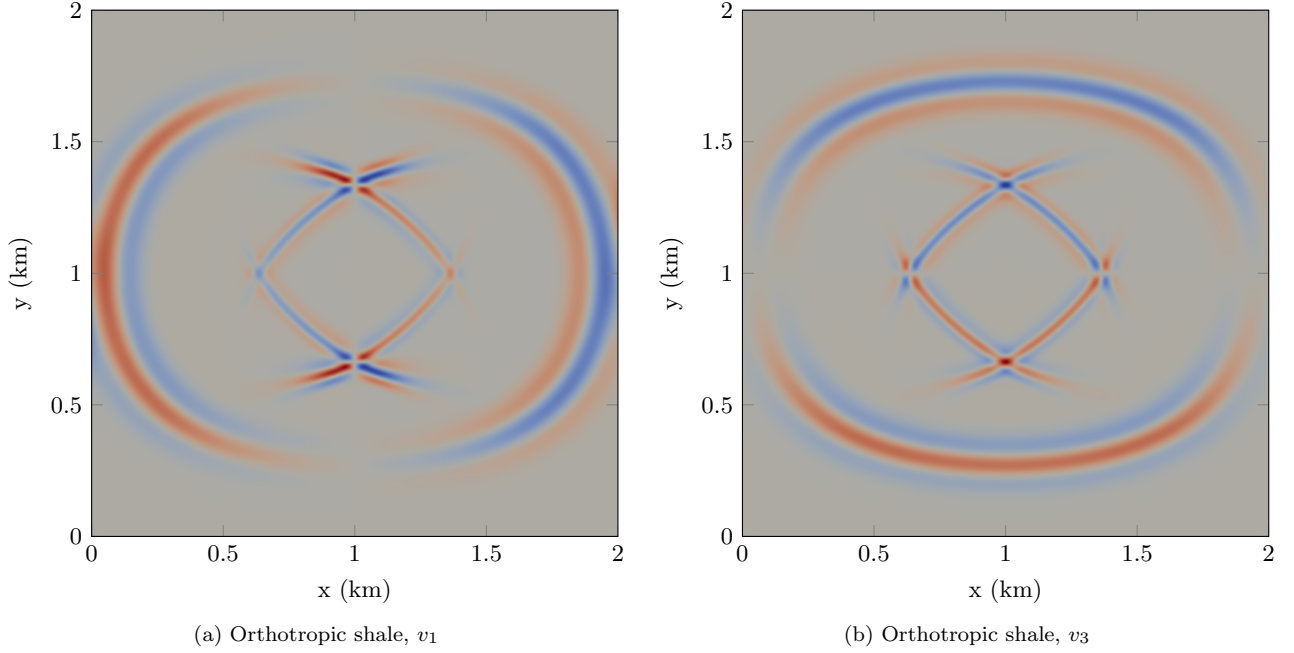


Figure 3: Snapshots of particle velocities in orthotropic shale (column 1 of Table 1), computed at $t = 0.22$ s, where (a) and (b) corresponds to v_1 and v_3 components. The central frequency of the forcing function is 20 Hz corresponding to the relaxation peak of materials. The point source is located in the center of the domain. The solution is computed using polynomials of degree $N = 3$ and $K = 32,768$.

we report relative L^2 errors for all components of the solution \mathbf{U}

$$\frac{\|\mathbf{U} - \mathbf{U}_h\|_{L^2(\Omega)}}{\|\mathbf{U}\|_{L^2(\Omega)}} = \frac{\left(\sum_{i=1}^m \|\mathbf{U}_i - \mathbf{U}_{i,h}\|_{L^2(\Omega)}^2\right)^{1/2}}{\left(\sum_{i=1}^m \|\mathbf{U}_i\|_{L^2(\Omega)}^2\right)^{1/2}}.$$

The error is computed for an isotropic sandstone. In Figure 2, we show the L^2 errors computed at $T=1$, using uniform triangular meshes constructed by bisecting an uniform mesh of quadrilaterals along the diagonal. Figure 2a shows error plots using the central flux with $\alpha = 0$ (CFL = 1). We observe convergence rate of $O(h^N)$ or $O(h^{N+1})$ for odd-even N . Figure 2b and 2c show errors for penalty fluxes with $\alpha = 0.5$ (CFL = 0.5), and 1 (CFL = 0.8), respectively. For $N = 1, \dots, 5$, $O(h^{N+1})$, rates of convergence are observed. We note that for $N = 4$ and $N = 5$, we observe results which are better than the 4th order accuracy of our time-stepping scheme. This is most likely due to the benign nature of the solution in time and the choice of time step (40) which scales as $O(h/N^2)$.

4.3. Application examples

We next demonstrate the accuracy and flexibility of the proposed DG method for several application-based problems in linear viscoelasticity with anisotropy. All computations are done using penalty parameters $\alpha = 0.5$ unless specified otherwise. In subsequent simulations, the forcing is applied to both the x - and z -components of stress i.e. $(\sigma_{11}, \sigma_{33})$.

$$f(\mathbf{x}, t) = (1 - 2(\pi f_0(t - t_0))^2) \exp[-(\pi f_0(t - t_0))^2] \delta(\mathbf{x} - \mathbf{x}_0), \quad (44)$$

where \mathbf{x}_0 is the position of the point source and f_0 is the central frequency.

In the following simulations, two types of elastic waves are observed: a P wave, and an S wave with an anisotropic dissipative phenomena.

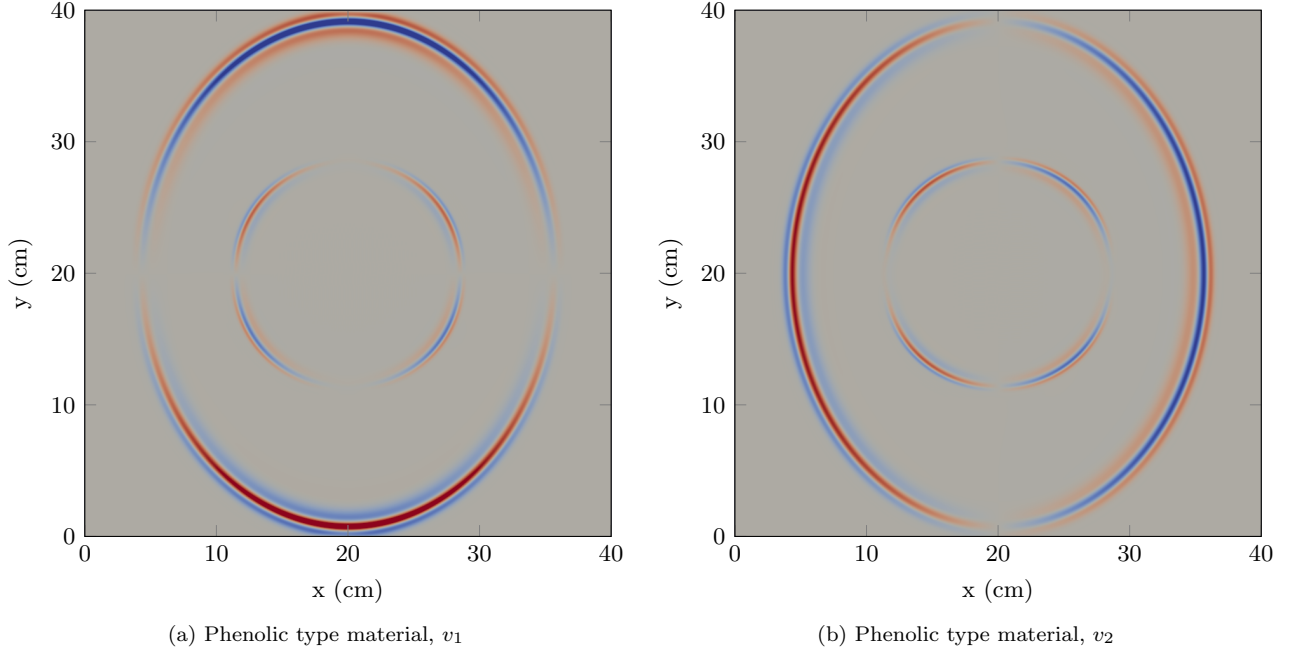


Figure 4: Snapshots of particle velocities in Phenolic material (column 2 of Table 1), computed at $t = 53.2 \mu\text{s}$, where (a) and (b) corresponds to v_1 and v_2 components. The central frequency of the forcing function is 250 kHz which also corresponds to relaxation peak of the material. The point source is located in the center of the domain. The solution is computed using polynomials of degree $N = 3$ and $K = 131,072$.

4.3.1. 2D Orthotropic shale

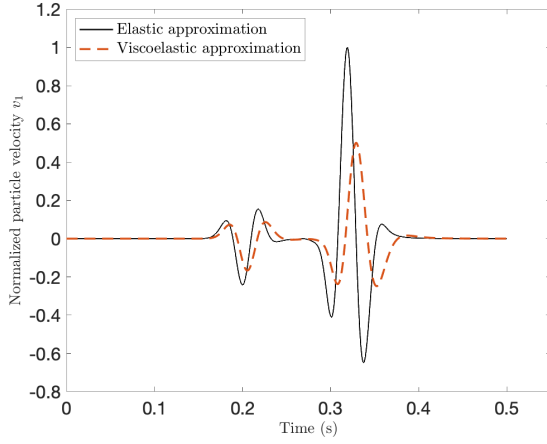
To illustrate the effect of anisotropic dissipation in a viscoelastic medium, we perform a computational experiment in orthotropic shale with material properties given in Table 1 (Column 1). The size of the computational domain is $2 \text{ km} \times 2 \text{ km}$. The domain is discretized with uniform triangular elements with a minimum edge length of 15.625 m. Figures 3(a)-(b) show the x - and z - components of the particle velocity of the orthotropic shale, respectively. The central frequency of the forcing function is $f_0 = 20 \text{ Hz}$, which is also the frequency for relaxation peak of the material. Polynomials of degree $N = 3$ are used for the simulation, and the propagation time is 0.22 s. Both wave modes can be observed: the P mode and the shear mode (S, inner wavefront). A shear wave cusp is clearly observed in Figure 3a and 3b.

4.3.2. 2D Phenolic material

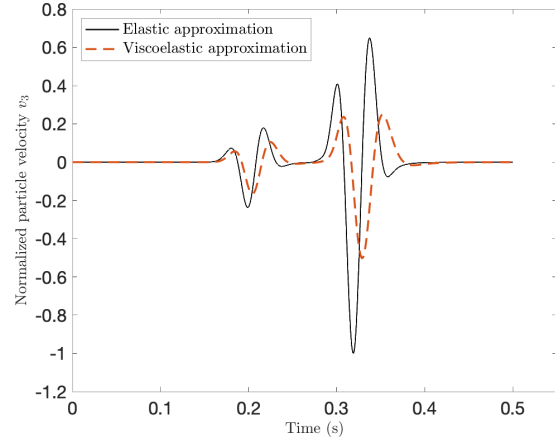
To further validate our numerical scheme, we perform a computational experiment in Phenolic material which has a high relaxation frequency of 250 kHz with material properties given in Table 1 (Column 2). The size of the computational domain is $40 \text{ cm} \times 40 \text{ cm}$. The domain is discretized with uniform triangular element with a minimum edge length of 0.1562 cm. Figures 4(a)-(b) represent the x - and z - components of the particle velocity of the Phenolic material, respectively. The central frequency of the forcing function is $f_0 = 250 \text{ kHz}$ (the frequency for relaxation peak). Polynomials of degree $N = 3$ are used for the simulation. The propagation time is $53.2 \mu\text{s}$. Both modes of waves can be observed: the P mode and the shear mode (S, inner wavefront).

4.3.3. Comparison of elastic and viscoelastic models

To show the effect of the attenuation on wave propagation, we compare numerical solutions of elastic and viscoelastic wave equation in an isotropic sandstone with material properties given in Table 1 (Column 3). Numerical solution are computed in a domain of dimension $[-1 \text{ km}, 1 \text{ km}] \times [-1 \text{ km}, 1 \text{ km}]$, and discretized

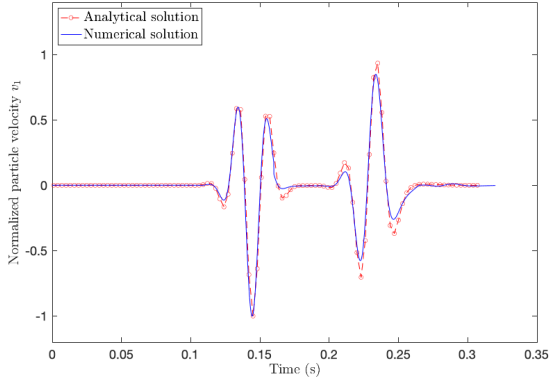


(a) v_1 for elastic and viscoelastic approximation

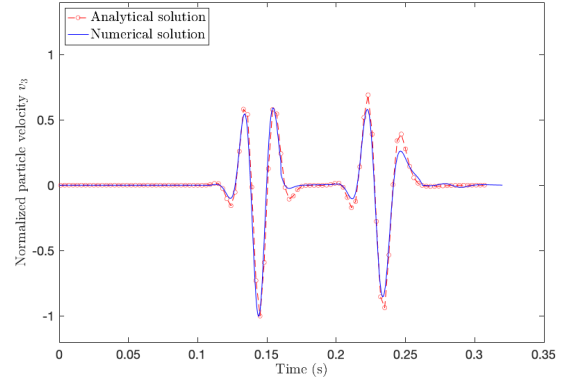


(b) v_3 for elastic and viscoelastic approximation

Figure 5: A comparison of the time history of particle velocities for both elastic and viscoelastic approximations. Subfigures (a) and (b) represent the horizontal and vertical particle velocities, respectively. A difference between elastic and viscoelastic approximation is clearly visible in both by phase and amplitude difference between the traces.



(a) Analytical vs numerical simulation for v_1



(b) Analytical vs numerical simulation for v_2

Figure 6: A comparison between numerical and analytical solution of viscoelastic wave equation in a homogeneous media. Subfigures (a) and (b) represent the horizontal and vertical particle velocities, respectively. Numerical solution is computed in 2D and for polynomials of degree $N = 3$.

with uniform triangular elements with a minimum edge length of 20.833 m. Figure 5 shows a comparison between the numerical solutions of particle velocities for elastic and viscoelastic equation with x - and z -components represented in Figure 5a and 5b, respectively. The central frequency of the forcing function is $f_0 = 20$ Hz. Polynomials of degree $N = 3$ are used for the simulation. The solution are stored at receiver position (250 m, 250 m) with source located at (0 m, 0 m). A difference between the amplitude of elastic and viscoelastic solutions in Figure 5 is due to the attenuation brought in to the system due to the relaxation. The relaxation also results into decreasing the velocity of waves (when compared against the pure elastic or lossless case), which is clearly reflected by the difference in phases between the elastic and viscoelastic solutions, shown in Figure 5.

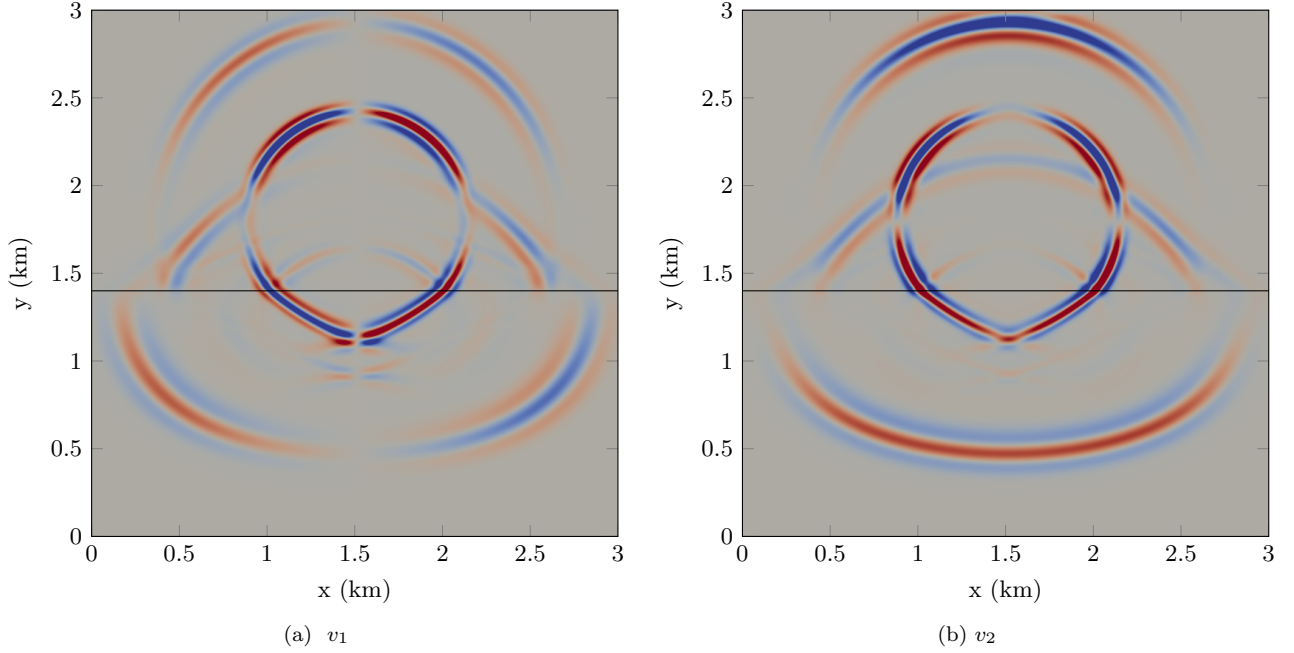


Figure 7: Snapshots of particle velocities in the layered model with (a) and (b) showing v_1 and v_2 components at $t = 0.4$ s. The central frequency of the forcing function is 20 Hz. The point source is located at (1.5 km, 1.8 km). The solution is computed using polynomials of degree $N = 3$ and $K = 32,768$.

4.3.4. Comparisons of analytical and numerical solutions

Now, we compare the analytical and numerical solution, computed from our DG method, of 2D viscoelastic wave equation. (31). The analytical solution of isotropic viscoelastic wave equation is computed by Carcione [3] using correspondence principle [45]. The derivation of analytical solution in a homogeneous and isotropic medium is given in Appendix B. The following forcing function is used to compute the analytical solution

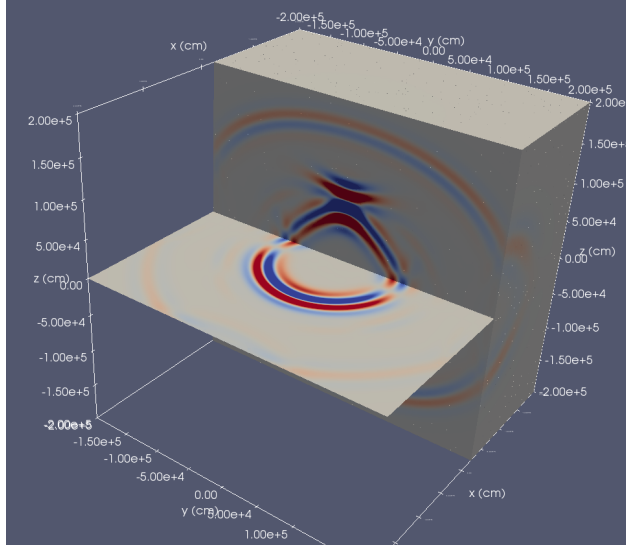
$$f(\mathbf{x}, t) = \exp \left[-\frac{\Delta\omega^2(t-t_0)^2}{4} \right] \cos[\bar{\omega}(t-t_0)] \delta(\mathbf{x} - \mathbf{x}_0), \quad (45)$$

where $\bar{\omega} = 2\pi f_0$ is central angular frequency with $\Delta\omega = \frac{\bar{\omega}}{2}$.

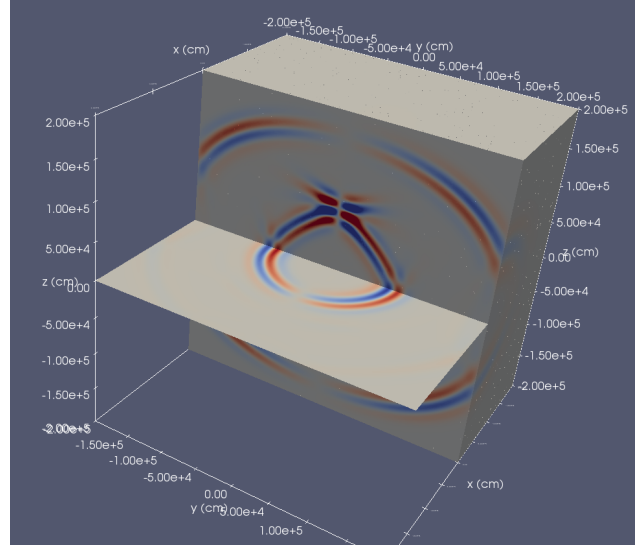
To compute the analytical solution one required the frequency spectrum of (45), which is expressed as

$$F(\omega) = \frac{\sqrt{\pi}}{\Delta\omega} \left(\exp \left[-\left(\frac{\omega + \bar{\omega}}{\Delta\omega} \right)^2 \right] + \exp \left[-\left(\frac{\omega - \bar{\omega}}{\Delta\omega} \right)^2 \right] \right) \exp(-i\omega t_0). \quad (46)$$

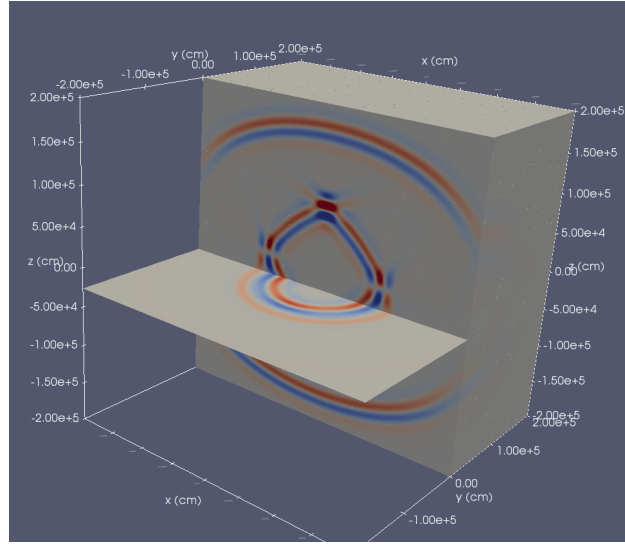
Equation (46) also satisfies the condition $F(\bar{\omega} + \Delta\omega) = F(\bar{\omega})/e$, which is the requirement to compute the analytical solution. Figures 6 shows a comparison between time histories of numerical and analytical solutions of viscoelastic wave equation with x - and z - components being represented in Figure 6a and 6b, respectively. Numerical solution are computed in a domain of dimension $[-0.5 \text{ km}, 0.5 \text{ km}] \times [-0.5 \text{ km}, 0.5 \text{ km}]$, which is discretized with uniform triangular elements with a minimum edge length of 4 m. The material properties of isotropic sandstone (Table 1, Column 3) is used to compute the solutions. The central frequency f_0 of forcing function is 45 Hz, which is located at (0 m, 0 m). The forcing function is added to the force corresponding to σ_{22} . Polynomials of degree $N = 3$ are used for the simulation. The solution is stored at the node with coordinate (250 m, 250 m). Figure 6a and 6b show a very good agreement between and analytical and numerical solutions and thus validating the accuracy of the proposed numerical method.



(a) v_1



(b) v_2



(c) v_3

Figure 8: Snapshots of particle velocities in a 3D homogeneous Orthotropic shale with material properties shown in columns 1 of Table 1. Sub figures (a), (b), and (c) are showing v_1 , v_2 and v_3 components at $t = 0.48$ s. The central frequency of the forcing function is 20 Hz. The point source is located at the center of the domain. The solution is computed using polynomials of degree $N = 3$ and $h = 32.5$ m.

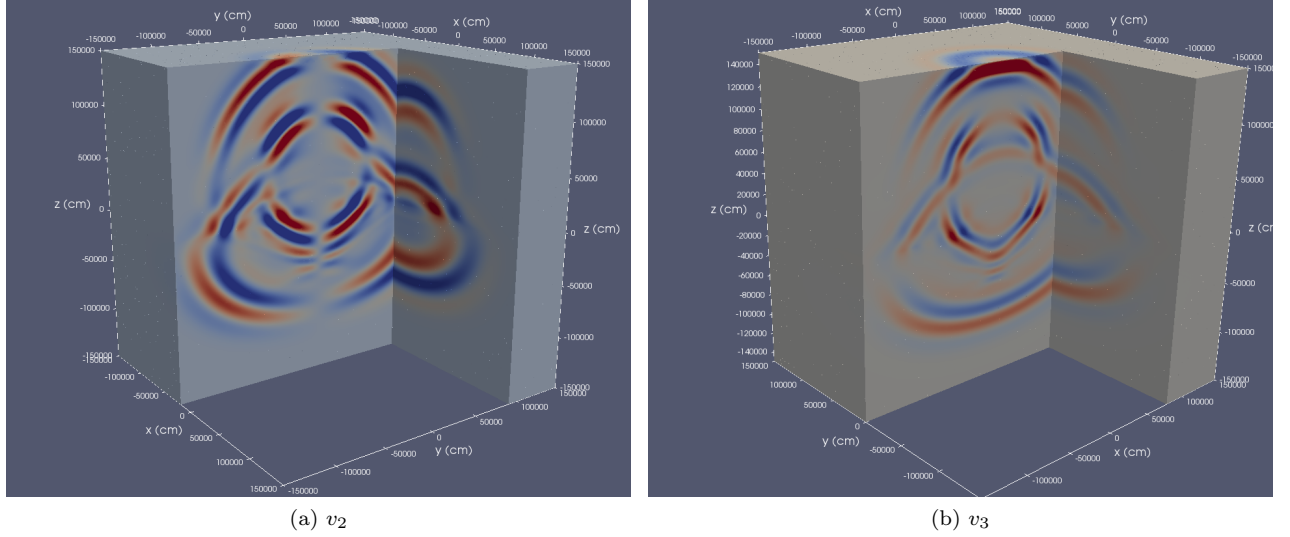


Figure 9: Snapshots of particle velocities in a 3D anisotropic heterogeneous two layer model of size $3 \text{ km} \times 3 \text{ km} \times 3 \text{ km}$. Sub figures (a), and (b) are represent v_2 and v_3 components at $t = 0.4 \text{ s}$. The central frequency of the forcing function is 20 Hz . The point source is located in the domain at $(0 \text{ km}, 0 \text{ km}, 0.3 \text{ km})$. The solution is computed using polynomials of degree $N = 3$ and $h = 32.5 \text{ m}$.

4.3.5. 2D Isotropic-anisotropic layered model

In this example, we illustrate the effect of an interface between two layers of viscoelastic media. In the layered model, the top and bottom layers correspond to isotropic sandstone and orthotropic shale, with material properties are given in Table 1 (Column 3 and Column 1). The size of the computational domain is $3 \text{ km} \times 3 \text{ km}$ in the x and z directions, respectively. The minimum edge size of the triangular elements used to mesh the domain is 23.4375 m . The point source is located at $(1.5 \text{ km}, 1.8 \text{ km})$ with a Ricker wavelet of frequency 20 Hz . The propagation time is 0.4 s . The simulation is performed using polynomials of degree $N = 3$. Snapshots of the x and z components of the particle velocity are shown in Figures 7a and 7b, respectively. Figure 7 clearly shows the direct, reflected, and transmitted wavefronts, corresponding to both P and S wave modes. The effect of anisotropy on all three modes is clearly seen as wavefronts move with different phase velocities.

4.3.6. 3D Orthotropic material

Now, we validate our numerical scheme for a 3D model. First, we perform a 3D computational experiment for orthotropic shale with the material properties given in Table 1 (Column 1). The size of the computational domain is $4 \text{ km} \times 4 \text{ km} \times 4 \text{ km}$ and is discretized by tetrahedral element with a minimum edge length of 32.5 m . The central frequency of the forcing function is $f_0 = 20 \text{ Hz}$ (the frequency for relaxation peak). Polynomials of degree $N = 3$ are used for the simulation. The propagation time is $0.48 \mu\text{s}$. Figures 8(a), (b) and (c) represent the x -, y - and z - components of the particle velocity of the orthotropic material, respectively. Both modes of waves can be observed: the P mode and the shear mode (S, inner wavefront). Figure 8 shows that the plane perpendicular to z - direction is a plane of symmetry, as wave propagation in the plane is isotropic.

4.3.7. 3D Isotropic-anisotropic layered model

In this example, we illustrate the effect of a two dimensional interface between two layers of the 3D viscoelastic media. The top and bottom layer of 3D model are comprised of isotropic sandstone and orthotropic shale, respectively. The size of the computational domain is $3 \text{ km} \times 3 \text{ km} \times 3 \text{ km}$ in the x , y and z directions, respectively. The minimum edge size of the triangular elements used to mesh the domain is

32.5 m. The point source is located at (0 km, 0 km, 0.4 km) with a Ricker wavelet of frequency 20 Hz. The propagation time is 0.4 s. The simulation is performed using polynomials of degree $N = 3$. Snapshots of the y and z components of the particle velocity are shown in Figures 9a and 9b, respectively. Figure 9 clearly demonstrate the effect the interface responsible for the direct, reflected, and transmitted wavefronts of P and shear waves present in the system.

4.4. A large 3D heterogeneous subsurface model

We use a 3D reservoir model from Shukla *et al.* [35]. The model is characterized by rock layers, discontinuity, and a surface with undulated topography. The discretized model is shown in Figure 10a. The dimension of the model is $(22.8 \times \text{km} \times 17.4 \text{ km} \times 8.0 \text{ km})$ in x , y and z directions, respectively. The domain is discretized with tetrahedral elements with a minimum edge length of 125 m. The top surface of the model is perturbed so that the effects of the topography, assumed as a free surface, could be incorporated into numerical simulations. Figure 10(b) represent the z - component of the particle velocity at 3.5 s. The central frequency of the forcing function is 20 Hz. Polynomials of degree $N = 3$ are used for simulation. The various modes of transmissions, reflections and scattering can be clearly seen in Figure 10b.

5. Conclusions

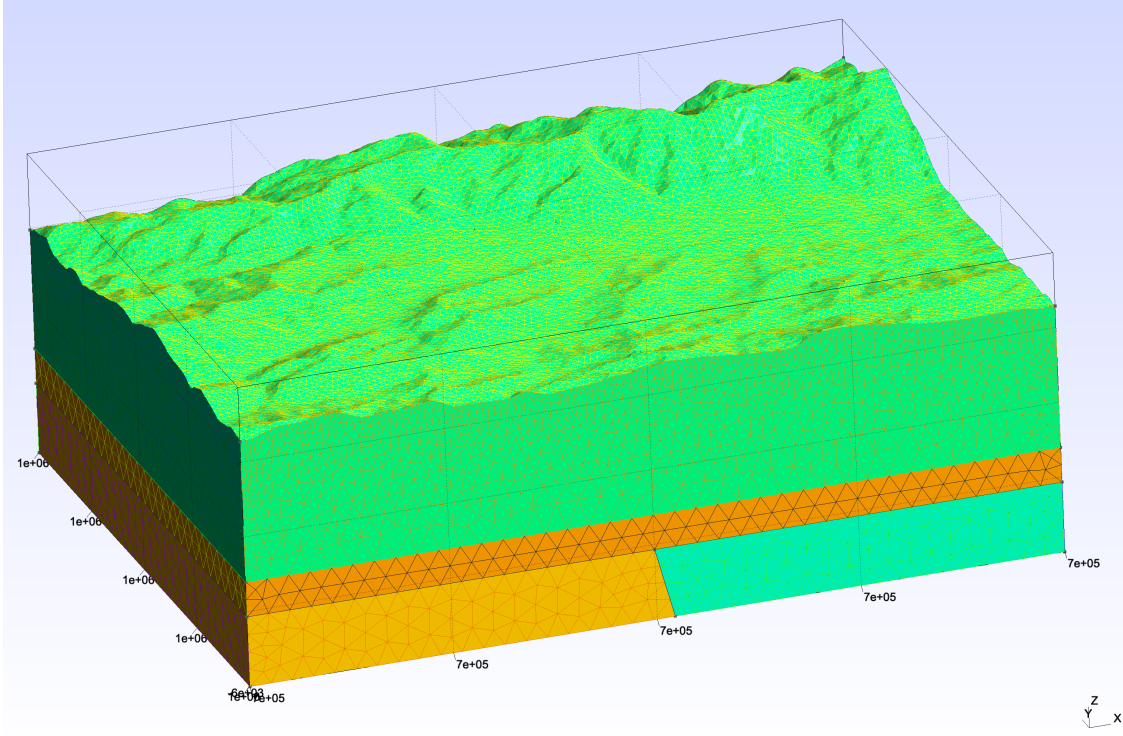
This work presents a high order discontinuous Galerkin method for a new symmetric form of the linear anisotropic viscoelastic wave equations. The method is energy stable and high order accurate for arbitrary stiffness tensors. We confirm the high-order accuracy of the numerical method using an analytic plane wave solution in a viscoelastic media. Finally, we provide computational results for various combinations of homogeneous and heterogeneous medium.

6. Acknowledgments

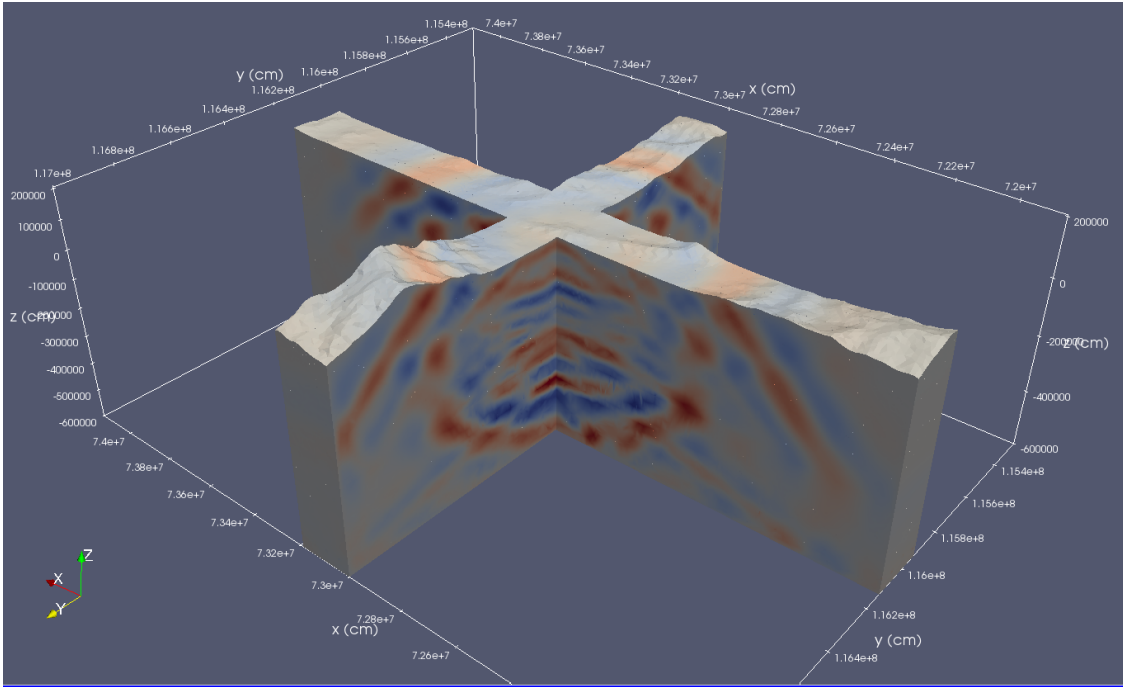
The authors gratefully thank the sponsors of the Geo-Mathematical Imaging Group at Rice University for providing the resources to carry out this work. Jesse Chan gratefully acknowledges support from the NSF under awards DMS-1719818 and DMS-1712639. MVdH gratefully acknowledges support from the Simons Foundation under the MATH + X program and the NSF under grant DMS-1815143. The authors gratefully acknowledge Dr. José M Carcione of INOGS Italy, for his help in deriving and implementing the analytical solution in a 2D viscoelastic medium.

References

- [1] B Hosten, M Deschamps, and Bernhard R Tittmann. Inhomogeneous wave generation and propagation in lossy anisotropic solids. application to the characterization of viscoelastic composite materials. *The Journal of the Acoustical Society of America*, 82(5):1763–1770, 1987.
- [2] Rob J Arts and Patrick NJ Rasolofosaon. Approximation of velocity and attenuation in general anisotropic rocks. In *SEG Technical Program Expanded Abstracts 1992*, pages 640–643. Society of Exploration Geophysicists, 1992.
- [3] JM Carcione. *Wave Fields in Real Media: Wave Propagation in Anisotropic, Anelastic, Porous and Electromagnetic Media*. Elsevier Science, 2014.
- [4] JM Carcione. Wave propagation in anisotropic linear viscoelastic media: Theory and simulated wave-fields. *Geophysical Journal International*, 101(3):739–750, 1990.
- [5] Morteza M Mehrabadi and Stephen C Cowin. Eigentensors of linear anisotropic elastic materials. *The Quarterly Journal of Mechanics and Applied Mathematics*, 43(1):15–41, 1990.



(a) 3D model constructed with topography with minimum edge length of element $h = 125$ m



(b) Snapshot of v_3 at $t = 3.5$ s

Figure 10: Snapshot of v_3 for a 3D heterogeneous model constructed with topography on the top surface and a discontinuity in lower most layer. Subfigure (a) shows the 3D model of domain size (22.8 km, 17.4 km 8.0 km) and discretized with tetrahedral element with a minimum edge length of element being $h = 125$ m. Subfigure (b) shows the snapshot of v_3 at 3.5 s. The point source is located in the domain at (11.4 km, -8.7 km, -50 m) . The solution is computed using polynomials of degree $N = 3$.

- [6] K Helbig. Foundations of anisotropy for exploration seismics. In *International Journal of Rock Mechanics and Mining Sciences and Geomechanics Abstracts*, volume 1, pages 19A–20A, 1996.
- [7] Jose M Carcione. Constitutive model and wave equations for linear, viscoelastic, anisotropic media. *Geophysics*, 60(2):537–548, 1995.
- [8] Peter Moczo, Jozef Kristek, and Martin Gális. *The finite-difference modelling of earthquake motions: Waves and ruptures*. Cambridge University Press, 2014.
- [9] Heiner Igel. *Computational Seismology: A Practical Introduction*. Oxford University Press, 2017.
- [10] Jean Virieux. P-SV wave propagation in heterogeneous media: Velocity-stress finite-difference method. *Geophysics*, 51(4):889–901, 1986.
- [11] Kurt J Marfurt. Accuracy of finite-difference and finite-element modeling of the scalar and elastic wave equations. *Geophysics*, 49(5):533–549, 1984.
- [12] Peter Moczo, Johan OA Robertsson, and Leo Eisner. The finite-difference time-domain method for modeling of seismic wave propagation. *Advances in Geophysics*, 48:421–516, 2007.
- [13] Thomas Bohlen. Parallel 3-D viscoelastic finite difference seismic modelling. *Computers & Geosciences*, 28(8):887–899, 2002.
- [14] Alan R Levander. Fourth-order finite-difference P-SV seismograms. *Geophysics*, 53(11):1425–1436, 1988.
- [15] John C Strikwerda. *Finite difference schemes and partial differential equations*, volume 88. Siam, 2004.
- [16] Robert Andrew Drainville, Laura Curiel, and Samuel Pichardo. Superposition method for modelling boundaries between media in viscoelastic finite difference time domain simulations. *The Journal of the Acoustical Society of America*, 146(6):4382–4401, 2019.
- [17] Ekkehart Tessmer and Dan Kosloff. 3-D elastic modeling with surface topography by a Chebychev spectral method. *Geophysics*, 59(3):464–473, 1994.
- [18] José M Carcione. Domain decomposition for wave propagation problems. *Journal of Scientific Computing*, 6(4):453–472, 1991.
- [19] Hesheng Bao, Jacobo Bielak, Omar Ghattas, Loukas F Kallivokas, David R O’Hallaron, Jonathan R Shewchuk, and Jifeng Xu. Large-scale simulation of elastic wave propagation in heterogeneous media on parallel computers. *Computer Methods in Applied Mechanics and Engineering*, 152(1-2):85–102, 1998.
- [20] Anthony T Patera. A spectral element method for fluid dynamics: laminar flow in a channel expansion. *Journal of Computational Physics*, 54(3):468–488, 1984.
- [21] G za Seriani and Enrico Priolo. Spectral element method for acoustic wave simulation in heterogeneous media. *Finite Elements in Analysis and Design*, 16(3):337–348, 1994.
- [22] Dimitri Komatitsch and Jean-Pierre Vilotte. The spectral element method: An efficient tool to simulate the seismic response of 2D and 3D geological structures. *Bulletin of the Seismological Society of America*, 88(2):368–392, 1998.
- [23] Jose M Carcione, Gérard C Herman, and APE Ten Kroode. Seismic Modeling. *Geophysics*, 67(4):1304–1325, 2002.
- [24] J.S. Hesthaven and T. Warburton. *Nodal discontinuous Galerkin methods: algorithms, analysis, and applications*, volume 54. Springer, 2007.
- [25] A. Klöckner, T. Warburton, J. Bridge, and J.S. Hesthaven. Nodal discontinuous Galerkin methods on graphics processors. *Journal of Computational Physics*, 228(21):7863–7882, 2009.

- [26] M. Ainsworth. Dispersive and dissipative behaviour of high order discontinuous Galerkin finite element methods. *Journal of Computational Physics*, 198(1):106–130, 2004.
- [27] L.C. Wilcox, G. Stadler, C. Burstedde, and O. Ghattas. A high-order discontinuous Galerkin method for wave propagation through coupled elastic–acoustic media. *Journal of Computational Physics*, 229(24):9373–9396, 2010.
- [28] M. Käser, M. Dumbser, J. De La Puente, and H. Igel. An arbitrary high-order discontinuous Galerkin method for elastic waves on unstructured meshes—III. Viscoelastic attenuation. *Geophysical Journal International*, 168(1):224–242, 2007.
- [29] J. de la Puente, M. Käser, M. Dumbser, and H. Igel. An arbitrary high-order discontinuous Galerkin method for elastic waves on unstructured meshes—IV. Anisotropy. *Geophysical Journal International*, 169(3):1210–1228, 2007.
- [30] R. Ye, M.V. de Hoop, C.L. Petrovitch, L.J. Pyrak-Nolte, and L.C. Wilcox. A discontinuous Galerkin method with a modified penalty flux for the propagation and scattering of acousto-elastic waves. *Geophysical Journal International*, 205(2):1267–1289, 2016.
- [31] L Lambrecht, A Lamert, W Friederich, T Möller, and MS Boxberg. A nodal discontinuous Galerkin approach to 3-D viscoelastic wave propagation in complex geological media. *Geophysical Journal International*, 212(3):1570–1587, 2018.
- [32] Marshall J Leitman and George MC Fisher. The linear theory of viscoelasticity (constitutive equations, creep laws, stress functions, variational principles and differential operators in dynamic and static linear viscoelasticity theory). *Solid-state mechanics 3.(A 73-45495 24-32) Berlin, Springer-Verlag, 1973,*, pages 1–123, 1973.
- [33] J. Chan. Weight-adjusted discontinuous Galerkin methods: Matrix-valued weights and elastic wave propagation in heterogeneous media. *International Journal for Numerical Methods in Engineering*, 113(12):1779–1809, 2018.
- [34] Jesse Chan, Russell J Hewett, and Timothy Warburton. Weight-adjusted discontinuous Galerkin methods: wave propagation in heterogeneous media. *SIAM Journal on Scientific Computing*, 39(6):A2935–A2961, 2017.
- [35] Khemraj Shukla, Jesse Chan, V Maarten, and Priyank Jaiswal. A weight-adjusted discontinuous Galerkin method for the poroelastic wave equation: penalty fluxes and micro-heterogeneities. *Journal of Computational Physics*, 403:109061, 2020.
- [36] Jean-Pierre Berenger. A perfectly matched layer for the absorption of electromagnetic waves. *Journal of Computational Physics*, 114(2):185–200, 1994.
- [37] Thomas Hagstrom and Timothy Warburton. A new auxiliary variable formulation of high-order local radiation boundary conditions: corner compatibility conditions and extensions to first-order systems. *Wave Motion*, 39(4):327–338, 2004.
- [38] J. Chan and T. Warburton. GPU-Accelerated Bernstein–Bézier Discontinuous Galerkin Methods for Wave Problems. *SIAM Journal on Scientific Computing*, 39(2):A628–A654, 2017.
- [39] K. Guo and J. Chan. Bernstein–Bézier weight-adjusted discontinuous Galerkin methods for wave propagation in heterogeneous media. *arXiv preprint arXiv:1808.08645*, 2018.
- [40] Mark H Carpenter and Christopher A Kennedy. Fourth-order 2N-storage Runge-Kutta schemes. Technical Report NASA-TM-109112, NASA Langley Research Center, 1994.

- [41] Jesse Chan, Zheng Wang, Axel Modave, Jean-Francois Remacle, and Tim Warburton. GPU-accelerated discontinuous galerkin methods on hybrid meshes. *Journal of Computational Physics*, 318:142–168, 2016.
- [42] Jesse Chan and T Warburton. On the penalty stabilization mechanism for upwind discontinuous galerkin formulations of first order hyperbolic systems. *Computers & Mathematics with Applications*, 74(12):3099–3110, 2017.
- [43] Eleuterio F Toro. The HLL and HLLC riemann solvers. In *Riemann solvers and numerical methods for fluid dynamics*, pages 315–344. Springer, 2009.
- [44] J. de la Puente, M. Dumbser, M. Käser, and H. Igel. Discontinuous Galerkin methods for wave propagation in poroelastic media. *Geophysics*, 73(5):T77–T97, 2008.
- [45] David Russell Bland. *The theory of linear viscoelasticity*. Courier Dover Publications, 2016.
- [46] G Eason, J Fulton, and Ian Naismith Sneddon. The generation of waves in an infinite elastic solid by variable body forces. *Philosophical Transactions of the Royal Society of London. Series A, Mathematical and Physical Sciences*, 248(955):575–607, 1956.

Appendix A. Inverse of compliance matrix C

The expressions for r_{ij} in (30) are

$$r_{11} = -\frac{(c_{11}c_{33} - c_{13}^2)}{(c_{11} - c_{12})(c_{11}c_{33} + c_{12}c_{33} - 2c_{13}^2)} \quad (\text{A.1})$$

$$r_{12} = -\frac{(c_{12}c_{33} - c_{13}^2)}{(c_{11} - c_{12})(c_{11}c_{33} + c_{12}c_{33} - 2c_{13}^2)} \quad (\text{A.2})$$

$$r_{13} = -\frac{c_{13}}{(c_{11}c_{33} + c_{12}c_{33} - 2c_{13}^2)} \quad (\text{A.3})$$

$$r_{33} = \frac{(c_{11} + c_{12})}{(c_{11}c_{33} + c_{12}c_{33} - 2c_{13}^2)} \quad (\text{A.4})$$

Appendix B. Analytic solution in a homogeneous viscoelastic media

The solution of the elastic wave equation in an 2-D isotropic medium for an impulsive point force is given by Eason *et al.* [46]. For a force acting in the positive x_3 -direction, displacement solutions are expressed as [3]

$$\begin{aligned} u_1(r, t) &= \left(\frac{F_0}{2\pi\rho} \right) \frac{xz}{r^2} [G_1(r, t) + G_3(r, t)], \\ u_3(r, t) &= \left(\frac{F_0}{2\pi\rho} \right) \frac{1}{r^2} [z^2 G_1(r, t) - x^2 G_3(r, t)], \end{aligned} \quad (\text{B.1})$$

where F_0 is a the magnitude of the force and $r^2 = x^2 + z^2$, and $G_1(r, t)$ and $G_3(r, t)$ are Green's function expresses as

$$\begin{aligned} G_1(r, t) &= \frac{1}{c_p^2} (t^2 - \tau_p^2)^{-1/2} H(t - \tau_p) + \frac{1}{r^2} (t^2 - \tau_p^2)^{1/2} H(t - \tau_p) - \frac{1}{r^2} (t^2 - \tau_s^2)^{1/2} H(t - \tau_s), \\ G_3(r, t) &= -\frac{1}{c_s^2} (t^2 - \tau_s^2)^{-1/2} H(t - \tau_s) + \frac{1}{r^2} (t^2 - \tau_p^2)^{1/2} H(t - \tau_p) - \frac{1}{r^2} (t^2 - \tau_s^2)^{1/2} H(t - \tau_s), \end{aligned} \quad (\text{B.2})$$

where $\tau_p = \frac{r}{c_p}$, $\tau_s = \frac{r}{c_s}$ with c_p and c_s being phase velocities of the compressional and shear waves. $H(t)$ is Heaviside function. To recover the anelastic solution the correspondence principle [3] is applied on

frequency domain representation of (B.2). We also use following identities of transform pairs of zero- and first-order Hankel function of the second kind

$$\begin{aligned} \int_{-\infty}^{\infty} \frac{1}{\tau^2} (t^2 - \tau^2)^{1/2} H(t - \tau) \exp(i\omega t) dt &= \frac{i\pi}{2\omega\tau} H_1^{(2)}(\omega\tau), \\ \int_{-\infty}^{\infty} \frac{1}{\tau^2} (t^2 - \tau^2)^{-1/2} H(t - \tau) \exp(i\omega t) dt &= -\frac{i\pi}{2\omega\tau} H_0^{(2)}(\omega\tau). \end{aligned} \quad (\text{B.3})$$

Now, Fourier transform of (B.2) with respect to time yields

$$\hat{G}_1(r, \omega, c_p, c_s) = -\frac{i\pi}{2} \left[\frac{1}{(c_p(\omega))^2} H_0^{(2)}\left(\frac{\omega r}{c_p}\right) + \frac{1}{\omega r c_s(\omega)} H_1^{(2)}\left(\frac{\omega r}{c_s(\omega)}\right) - \frac{1}{\omega r c_p(\omega)} H_1^{(2)}\left(\frac{\omega r}{c_p(\omega)}\right) \right], \quad (\text{B.4})$$

$$\hat{G}_3(r, \omega, c_p, c_s) = \frac{i\pi}{2} \left[\frac{1}{(c_s(\omega))^2} H_0^{(2)}\left(\frac{\omega r}{c_s(\omega)}\right) - \frac{1}{\omega r c_s(\omega)} H_1^{(2)}\left(\frac{\omega r}{c_s(\omega)}\right) + \frac{1}{\omega r c_p(\omega)} H_1^{(2)}\left(\frac{\omega r}{c_p(\omega)}\right) \right], \quad (\text{B.5})$$

where $c_p(\omega) = \sqrt{\frac{(c_{11} + c_{33})M_1(\omega) + c_{33}M_2(\omega)}{\rho}}$, and $c_s(\omega) = \sqrt{\frac{c_{33}M_2(\omega)}{\rho}}$ where M_1 and M_2 are recovered from (12), which for isotropic case are as follows,

$$M_{\nu \in \{1,2\}} = \frac{\tau_{\sigma}^{(\nu)}}{\tau_{\epsilon}^{(\nu)}} \left(\frac{1 + i\omega\tau_{\epsilon}^{(\nu)}}{1 + i\omega\tau_{\sigma}^{(\nu)}} \right).$$

Now, taking the Fourier transform of (B.1) and using (B.4) and (B.5), we get

$$\begin{aligned} u_1(r, \omega, c_p, c_s) &= \left(\frac{F_0}{2\pi\rho} \right) \frac{xz}{r^2} \left[\hat{G}_1(r, \omega, c_p, c_s) + \hat{G}_3(r, \omega, c_p, c_s) \right] \\ u_3(r, \omega, c_p, c_s) &= \left(\frac{F_0}{2\pi\rho} \right) \frac{1}{r^2} \left[z^2 \hat{G}_1(r, \omega, c_p, c_s) - x^2 \hat{G}_3(r, \omega, c_p, c_s) \right] \end{aligned} \quad (\text{B.6})$$

To ensure that solution is real in time, we express (B.6) as

$$u_{1,3}(\omega) = \begin{cases} u_{1,3}(r, \omega, c_p, c_s), & \omega \geq 0, \\ u_{1,3}^*(r, -\omega, c_p, c_s), & \omega < 0, \end{cases} \quad (\text{B.7})$$

where asterisk (*) denotes the complex conjugate. Multiplying (B.7) with frequency domain representation of a source time function and then taking the inverse Fourier transform will yield time-domain analytical displacement solution of 2D viscoelastic wave equation (31). The \hat{G}_1 and \hat{G}_3 are considered as zeros due to Hankel's functions being singular.